Late Pleistocene thrust tectonics in the north Peruvian forearc revealed by Terrestrial Cosmogenic Nuclides surface exposure dating, field structural data and seismic profiles

Andréa Peuzin, Marianne Saillard, Nicolas Espurt, Régis Braucher, Marc Régnier, Guillaume Duclaux, Laurence Audin, Adriana Lemgruber-Traby, Olivier Bellier, Jean-Claude Hippolyte, et al.

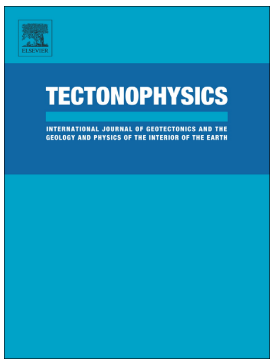

Late Pleistocene thrust tectonics in the north Peruvian forearc revealed by Terrestrial Cosmogenic Nuclides surface exposure dating, field structural data and seismic profiles

Andréa Peuzin, Marianne Saillard, Nicolas Espurt, Régis Braucher, Marc Régnier, Guillaume Duclaux, Laurence Audin, Adriana Lemgruber-Traby, Olivier Bellier, Jean-Claude Hippolyte, Ysabel Calderon

PII: S0040-1951(25)00184-2

DOI: https://doi.org/10.1016/j.tecto.2025.230798

Reference: TECTO 230798

To appear in: *Tectonophysics*

Received date: 13 September 2024

Revised date: 16 May 2025

Accepted date: 17 May 2025

Please cite this article as: A. Peuzin, M. Saillard, N. Espurt, et al., Late Pleistocene thrust tectonics in the north Peruvian forearc revealed by Terrestrial Cosmogenic Nuclides surface exposure dating, field structural data and seismic profiles, *Tectonophysics* (2024), https://doi.org/10.1016/j.tecto.2025.230798

Late Pleistocene thrust tectonics in the north Peruvian forearc revealed by Terrestrial Cosmogenic Nuclides surface exposure dating, field structural data and seismic profiles

Andréa Peuzin[1*], Marianne Saillard[1], Nicolas Espurt[1], Régis Braucher[2], Marc Régnier[1], Guillaume Duclaux[1], Laurence Audin[3], Adriana Lemgruber-Traby[4], Olivier Bellier[2], Jean-Claude Hippolyte[2] and Ysabel Calderon[5]

[1]Université Côte d'Azur, IRD, CNRS, Observatoire de la Côte d'Azur, Géoazur, Valbonne, France (peuzin@geoazur.unice.fr; saillard@geoazur.unice.fr; espurt@geoazur.unice.fr; regnier@geoazur.unice.fr ; duclaux@geoazur.unice.fr)

[2]Aix-Marseille Université, CNRS, IRD, INRAE, CEREGE, Aix-en-Provence, France (braucher@cerege.fr; bellier@cerege.fr; hippolyte@cerege.fr)

[3]Université Grenoble-Alpes, IRD, CNRS, ISTerre, Grenoble, France

(laurence.audin@ird.fr)

[4]IFP Energies Nouvelles, 1–4 Avenue du Bois Préau, 92852, Rueil Malmaison, France (adriana.traby@ifpen.fr)

[5]PERUPETRO S.A., Avenida Luis Aldana 320, San Borja, Lima 41, Peru

(ycalderon@perupetro.com.pe)

*Corresponding author: peuzin@geoazur.unice.fr

Keywords: ^{10}Be and ^{26}Al cosmogenic isotopes; alluvial fans; active shortening; morpho-tectonic markers; Northern Andean forearc;

Abstract

Precise dating of geomorphic markers that are subject to thrust-related deformation, such as alluvial fan surface are crucial for quantifying forearc deformation, especially in a context of weak interseismic coupling on the subduction interface as in northern Peru. In this study,

we document the late Pleistocene tectonic history of the Amotape massif, which is a prominent basement relief in the northern Peruvian forearc. To achieve this, we combine a morphometric analysis and Terrestrial Cosmogenic Nuclides (TCNs) surface exposure dating of alluvial fan surface with subsurface structural data. TCNs (^{10}Be and ^{26}Al) surface exposure ages of alluvial fan surfaces on the northwestern flank of the massif range from 35.1 ± 1.1 ka to 59.3 ± 2.1 ka for ^{10}Be and from 27.3 ± 2.0 ka to 48.9 ± 2.5 ka for ^{26}Al. Both cosmogenic nuclides provide consistent results. We calculated a mean weighted age of 39.0 ± 0.3 ka for an alluvial fan that is offset by a major NW-verging thrust. Our results provide an estimated slip rate of 1.15 ± 0.46 m/ka along the Amotape thrust front since the late Pleistocene. The surface deformation along the Amotape thrust front correlates with the top portion of a deep-seated contractional wedge involving the crustal basement, according to subsurface structural data and regional seismicity. This integrated analysis demonstrates active shortening in the onshore crustal basement of the northern Peruvian forearc where no active thrust reaching the surface has been described before.

1. Introduction

Unravelling active fault traces and the precise determination of their recent displacement, in particular on thrust with relatively low slip-rates (less than a few m/ka), remains a major challenge. This challenge is particularly acute along the active Andean margin of northern Peru, where paleosurfaces are frequently exposed to intense surface processes driven by extreme climatic events, such as El Niño-Southern Oscillation type events (ENSO-type events; Jamšek Rupnik et al., 2024). These events trigger prolonged periods of heavy rainfall (Wells, 1987; Ortlieb and Macharé, 1993; Vuille et al., 2000; Sanabria et al., 2017), resulting in increased erosion and sedimentation processes. Nevertheless, an analysis of the surfaces of alluvial fan deposits (e.g., Avouac et al., 1993; Heermance et al., 2008; Pang et al., 2021) are carried out on the northern Peruvian forearc to better understand Quaternary tectonic

evolution. Alluvial fans, as informative landforms, often develop in front of faulted massifs or structural highs in arid and semi-arid regions. They are valuable proxies for regional tectonic studies (e.g., Harvey et al., 1999, Quigley et al., 2007, Hedrick et al., 2013) and could provide insights into complex patterns of deformation at depth. In addition, pioneering studies on major Asian active faults have demonstrated that the Terrestrial Cosmogenic Nuclides (TCNs) dating method (^{10}Be and ^{26}Al) is a robust tool for dating alluvial fan surfaces, whose offsets provide the longest records of recent cumulative displacement (Tapponier et al., 2001). This method is therefore particularly appropriate for determining long-term (10–100 ka) slip rates of recent deformation (Burbank and Anderson, 2011). Despite low to moderate level of historical crustal seismicity in the northern Peruvian forearc (**Fig. 1b**; Beauval et al., 2013), no surface trace of active structures has yet been identified. Furthermore, Espurt et al. (2018) hypothesized the existence of a contractional structure adjacent - and below - to the western edge of the Amotape massif based on the substantial structural high observed within the forearc and additional geological field observations (**Fig. 1**). The aim of this study is therefore to search for evidence of the contractional structure and analyse potentially active tectonics along the western edge of the Amotape massif. This study contributes to the ongoing debate on the tectonic regime observed in the northern Peruvian forearc, between normal fault-dominated to thrust-dominated (Clift et al., 2003; Collot et al., 2002; Hoffmann-Rothe et al., 2006; Espurt et al., 2018).

We present new evidence of active surficial contractional structures corresponding to the northwestern thrust front of the Amotape massif using surface and subsurface data (**Fig. 1d**). To provide the timing of deformation and highlight the thrust activity of the Amotape massif, we performed surface exposure ages using ^{10}Be and ^{26}Al nuclides cosmogenic deformed alluvial fan surfaces. The data obtained offer insight into the late Pleistocene cumulative displacement along the thrust front of the Amotape massif, providing a valuable overview of

forearc deformation over this period. By combining fault slip and seismic reflection data in the underlying Eocene substratum together with regional seismicity data, our results allow to propose a new structural model of the western Amotape thrust front and estimate its active shortening during the late Pleistocene, a phenomenon that has been poorly described in the coastal forearc domain of northern Peru.

2. Study area

2.1 Tectonic context

Along the active margin of northern Peru, the Nazca Plate is subducting N83°E-ward beneath the Northern Andes at a velocity of 60 mm/a (Villegas-Lanza et al., 2016; **Fig. 1a**). Numerous large-scale geodetic analyses in Peru and Ecuador show that the northern Peruvian forearc system currently belongs to the Inca Sliver or micro-plate, moving SE-ward at a velocity of 4.4 mm/a (Chlieh et al., 2014; Nocquet et al., 2014; Villegas-Lanza et al., 2016). The northern Peruvian forearc zone incorporates a 1,000 km-long stable subduction segment, which is distinguished by a low interseismic coupling on the subduction interface. Consequently, subduction slip is characterised by creeping and stability (Chlieh et al., 2014; Nocquet et al., 2014; Villegas-Lanza et al., 2016). This slip mode is consistent with the historical seismicity of the northern Peruvian forearc, which has not experienced megathrust earthquakes in recent history. Only two moderate-magnitude events have been recorded in this region (Mw 7.5 in 1953 and Mw 7.1 in 1970; **Fig. 1b;** Beauval et al., 2013). Furthermore, seismicity provides additional information on subduction dynamics, revealing the presence of a flat subducting plate at a depth of around 100 km (Tavera et al., 2006; Hayes et al., 2018).

The morphostructural deformation of the northern Peruvian forearc system is characterized by three NW-verging prominent thrust-related structural highs (Banco Peru, Carpitas-Zorritos and Amotape from NW to SE) made of mixed continental, oceanic materials and off-scrapped strata (**Fig. 1b, c, d**; Fernández et al., 2005; Vega, 2009; Auguy et

al., 2017; Calvès et al., 2017; Espurt et al., 2018). These thrust wedges mark the boundaries of two major Cenozoic forearc depocenters filled by thick siliciclastic strata, the onshore Talara basin and the offshore Tumbes basin (**Fig. 1b, d)**. The sedimentary pile of these depocenters is deformed by numerous listric normal faults, gravitational raft tectonic instabilities and strike-slip faults (**Fig. 1d**; Vega, 2009; Cobos, 2010; Witt and Bourgois, 2010; Espurt et al., 2018; Peuzin et al., 2023). Belonging to the southeastern edge of the Talara basin, the Amotape massif consists of metamorphic and granitic Paleozoic-Triassic basement rocks unconformably overlain by Cretaceous or lower Eocene strata. (Espurt et al., 2018). However, the Amotape massif is elevated on the southern edge of the Talara basin, suggesting that the Amotape massif might overthrusts the Eocene Talara basin (Espurt et al., 2018; **Fig. 1c**).

2.2 Amotape massif: Breita and Gramadal areas

The Amotape massif is a prominent range located along the Talara basin (**Fig. 1b**), reaching elevations of approximately 1500 m above sea level (asl) and spanning latitudes between 4.04°S and 4.48°S (**Fig. 1b**). The northwestern flank of the Amotape massif is characterized by a system of interpreted as Quaternary (~2.6 Ma to present-day) coalescing alluvial fans located at different elevations, drained and incised by intermittent rivers (*i.e., arroyos* or normally dry drainage channels; **Figs. 1d and 2**). This study focuses on two main areas located along the Amotape massif and 30 km apart: the southern Breita area (4.25° south latitude, 80.88° west longitude) drained by the Breita River and the northern Gramadal area (4.03° south latitude, 80.59° west longitude; **Figs 1d and 2**) drained by the Gramadal River. The Breita and Gramadal areas were specially selected along the NW edge of the Amotape massif due to their accessibility and the presence of well-preserved alluvial fans. These alluvial fans, while extensively preserved in the Breita area, exhibit a lesser degree of preservation in the Gramadal area.

The Breita area, covering an area of ~5 km^2 is situated at a mean elevation of 238 m and, is characterized by supposed Quaternary alluvial fan deposits derived from the Paleozoic metamorphic strata of the nearby Amotape massif, which unconformably overlie Eocene strata of the Talara basin (**Fig. 2a**). An intermittent, discontinuous river network **(**i.e., *arroyos*) results in limited incision in the alluvial fan surfaces. Consequently, the incised riverbeds are shallow, with a maximum height of ~1 meter (**Figs. 1d and 2a**).

The Gramadal area, situated at a mean elevation of 300 m, is located 30 kilometers northwest of the Breita area and covers an area of approximately 3 km^2 (**Fig. 1d**). This area is characterized by alluvial fans also interpreted as Quaternary in age, overlying Eocene strata and are located 85 meters above the Gramadal riverbed (**Figs. 1d and 2b**). The alluvial fans contain large granite boulders of various sizes, derived from the Amotape massif. These large boulders are indicative of transport by high-energy flows that occur during extreme climatic events (*e.g.*, Echevin et al., 2018).

3. Methods

Field investigations were conducted along the northwestern edge of the Amotape massif, focusing on the Breita and Gramadal areas. The objective was to collect geomorphic markers (i.e., alluvial fan surfaces) and structural data as striated fault plane data in these areas (**Figs. 1d and 2**). These field observations and *in-situ* measurements were then integrated with geophysical data.

3.1 Geomorphological analysis

Geological and geomorphological mapping has been carried out to identify alluvial fans and to study the tectonic imprint at both regional and local levels. This includes an analysis of structures and landforms and satellite images. Furthermore, we combine geological and geomorphological observations based on field data with high-resolution digital elevation model (DEM) analyses. A 3-meter-resolution DEM (WorldDEM Neo from © DLR e.V.

2017-2021 and ©Airbus Defense and Space GmbH 2023) has been derived from multi-stereoscopic optical images acquired by the Pleiades satellite. We supplemented the WorldDEM Neo with a 3-arc sec-resolution DEM from the Shuttle Radar Topography Mission (SRTM) database (https://www.earthdata.nasa.gov/sensors/srtm; **Figs. 1d and 2a**). Unravelling tectonic imprints are often difficult when geomorphological expressions are subtle owing to the competition between tectonics and erosional processes. To extract this information, we therefore used TerraceM (Jara-Muñoz et al., 2016), a graphical interface in MATLAB®, to analyse the topography with swath profiles from the high-resolution DEM.

3.2 ^{10}Be and ^{26}Al Terrestrial Cosmogenic Nuclide dating

To date alluvial fan surfaces along the thrust front of the Amotape massif, we used TCNs surface exposure dating based on *in situ*-produced ^{10}Be and ^{26}Al concentrations measurements in different type of samples, including quartzite clasts, gravel, arenitic soil and plurimetric-size weathered boulders. These samples were collected at the surface of the alluvial fans (**Fig. 1d**). For a complete review of *in situ*-produced cosmogenic techniques, one can refer to Gosse and Phillips (2001) and Balco et al. (2008). This method has been widely applied to determine the age, style and rates of tectonic deformation at the Earth's surface throughout the Quaternary period (Benedetti and Van Der Woerd, 2014; and references therein). The existing literature provides numerous examples of applications that aimed at constraining slip rates of active faults. These applications can be categorized into two broad approaches: the direct dating of exhumed fault scarps (Benedetti et al., 2013) and the geomorphological assessment of deformation rates through the dating of tectonically offset alluvial fans (e.g., Jackson et al., 2002; Chevalier et al., 2012; Hetzel, 2013). Geomorphological assessment of deformation rates, achieved by dating tectonically offset markers, offers a significant advantage over direct methods. This approach facilitates the identification of long-term active deformation in a specific area of interest, leading to a better understanding of deformation processes. In

contrast, direct dating methods are limited to the identification of one or more discrete events, as fault scarps often preserve only a few events, making it difficult to determine long-term tectonic slip rates from these features. In the case of this study, it was difficult to identify datable morpho-tectonic markers. However, the quasi-horizontal, superficially incised alluvial fan surfaces, which minimise post-depositional processes affecting the original surface, are well preserved and presents few anthropogenic modifications. The alluvial fan deposits in the study area, which are interpreted to be Quaternary in age, exhibit high levels of induration and silica content (**Fig. 2**). The preserved upper surfaces are well-adapted for *in-situ* TCNs surface exposure dating method, which dates the abandonment of the alluvial fan.

3.2.1 Sampling strategy

To investigate the abandonment age of the alluvial fans in the Breita and Gramadal areas, a sampling strategy was applied. The interpreted as Quaternary alluvial deposits consist of a medium to coarse sand matrix supported, mainly angular to subrounded quartz-rich cobbles and pebbles and form decimeter-thick coarse beds. In total, seven surface samples were collected for ^{10}Be and ^{26}Al TCNs dating (**Fig. 3**). TCN dating was reliable because (1) surface of alluvial fans was sampled along the Amotape massif on a nearly flat site with a little to moderate surface incision (**Figs 1d, 2 and 3**) and (2) the interpreted as Quaternary fan deposits are well indurated and the quartz-rich cobbles and pebbles present at the surface are well embedded, ensuring that we sampled the original alluvial fan system. Finally, to minimize influence of inheritance or transport on dating, samples were selected if there were strongly embedded in the alluvial fan surface with no evidence of being part of reworked materials. In addition, clasts exhibiting well-developed cover of iron oxide or manganese varnish were targeted preferentially, as these observations are indicative of preserved surfaces and are consistent with assumption of the abandonment of surfaces of the alluvial fans (David and Thomas, 2008).

Quartzite clasts and gravels from alluvial fan surfaces were collected in the Breita area (alluvial fan surfaces Ia, Ib, Ic, with samples MA19-15, 16 and 17, respectively; **Figs 2a and 3a**). In the Gramadal area, the alluvial fan system is characterized by granite boulders of more than 4 meters in diameter, derived from Triassic granitoid intrusions in the Amotape massif (Fernández et al., 2005; **Fig. 3b**). These boulders are distributed and embedded at the top of the alluvial fan deposits. In this area, we collected arenitic soil and quartzite clast samples (MA19-23 and 24, respectively) from the top surface of the alluvial fan, and two other samples (MA19-25 and 26) from plurimetric-size weathered boulders in alluvial fan II (**Fig. 3b**).

3.2.2 ^{10}Be and ^{26}Al measurements, exposure ages and denudation rates calculations

All chemical preparation samples analyzed for ^{10}Be and ^{26}Al were performed at the National Laboratory of the Cosmogenic Nuclides (LN2C) at CEREGE (Aix-en-Provence, France). Quartz mineral was separated other minerals and purified from the samples to prepare target for accelerator mass spectrometer (AMS) analysis of ^{10}Be and ^{26}Al. All samples were crushed and sieved before beginning the analytical chemical protocol. The ^{10}Be and ^{26}Al extraction method serves to isolate and purify quartz, while simultaneously removing atmospheric ^{10}Be. Approximately 0.45 g of spike at 997 ppm was added, and beryllium was separated obtained after dissolution and precipitation in HF by successive anionic and cationic exchanges (Merchel et al., 1999). All final precipitates were then dried and heated to 800°C in order to obtain the respective beryllium and aluminium oxides. Following chemical purification and extraction, beryllium oxides were combined with niobium powder. All samples were then put into copper cathodes for Accelerator Mass Spectrometry (AMS) analyses. The AMS measurements were also performed at the French AMS National Facility, ASTER, at CEREGE (Arnorld et al., 2010). ^{10}Be data were calibrated from an ASTER in-house preparation "STD11", with a ^{10}Be/^{9}Be ratio of (1.191 ± 0.013) x 10^{-11} (Braucher et al.,

2015) using a ^{10}Be half-life of (1.387 ± 0.0012) x 10^6 years (Chmeleff et al., 2010; Korschinek et al., 2010). ^{26}Al/^{27}Al ratios were calibrated with an ASTER in-house preparation "SM-AL-11" of (7.401 ± 0.064) x 10^{-12} ratio (Merchel and Bremser, 2004) using a ^{26}Al half-life of (7.05 ± 0.17) x 10^5 years (Samworth et al., 1972). Reported analytical uncertainties include counting statistics and machine stability (~0.5 % for ^{10}Be; Arnold et al., 2010).

To derive exposure ages and denudation rates from measured cosmogenic ^{10}Be and ^{26}Al concentrations, we used the following equation

$$N(x,\varepsilon,t) = \frac{P_{s\rho}\cdot \exp(-x/L_n)1-\exp(-t(\varepsilon/L_n+\lambda)}{\varepsilon/L_n+\lambda}$$

$$+\frac{P_{\mu slow}\cdot \exp(-x/L_{\mu slow})1-\exp(-t(\varepsilon/L_{\mu slow}+\lambda)}{\varepsilon/L_{\mu slow}+\lambda}$$

$$+\frac{P_{\mu fast}\cdot \exp(-x/L_{\mu fast})1-\exp(-t(\varepsilon/L_{\mu fast}+\lambda)}{\varepsilon/L_{\mu fast}+\lambda}$$

where $N(x,\varepsilon,t)$ is the nuclide concentration as a function of depth x (g·cm^{-2}), denudation rate ε (g·cm^{-2} a^{-1}) and exposure time (t). $P_{s\rho}$, $P_{\mu slow}$, $P_{\mu fast}$ and L_n, $L_{\mu slow}$, $L_{\mu fast}$ are the production rates and attenuation lengths of neutrons, slow muons and fast muons, respectively. L_n, $L_{\mu slow}$, $L_{\mu fast}$ values used in this paper are 160, 1500 and 4320 g·cm^{-2}, respectively (Braucher et al., 2011), and λ is the radioactive decay constant of the TCN under investigation (^{10}Be, ^{26}Al). We applied a globally calibrated cosmogenic nuclides production rate of 4.02 ± 0.04 at/g at sea level and high latitude. This production rate was scaled at the geographical and altitudinal location of the sampling site using Stone (2000) polynomial and when necessary corrected for topographic shielding effect. A density estimates of 2.5 g/cm^3 for the quartz and granite was used.

The stated uncertainties of ages were determined through propagation of analytical errors on ^{10}Be and ^{26}Al measurements. The ages exhibit an overlap within the 1 sigma level of

uncertainties, which corresponds to the standard deviation of the measurements and the uncertainties on the production rates.

We calculated the TCNs surface exposure minimum age assuming no denudation and the maximum denudation rate assuming infinite exposure time. This approach, which does not account for potential inheritance as a depth profile would have been required to better constrain inheritance. Finally, to examine the statistical significance of TCNs surface exposure minimum age and maximum denudation rates, outliers were identified applying the reduced chi-square statistic for each sample (Ward and Wilson, 1978). The results are summarized in **Table 1**

3.3 Surface and subsurface structural data

In order to determine the stress regime and the Amotape thrust transport direction (Angelier, 1984; 1990), fault slip data were collected in the Breita area. Striated fault surfaces in lower Eocene strata were measured in three sites and paleo-stress trends (maximum horizontal stress axes sigma 1) were computed using the Angelier method (INVD method, Angelier, 1990). In addition, seismic reflection profiles and exploration well data (Vincente-1-X) west of the Breita area provide constraints on the structural architecture at depth and the kinematics of the Amotape massif-Talara basin transition (see **Supplementary material 2**).

4. Results

4.1 TCNs dating results

Based on ^{10}Be and ^{26}Al concentrations, we calculated minimum exposure ages and maximum denudation rates (**Table 1**), ignoring potential inheritance. In the Breita area, we sampled alluvial fan surfaces in three localities, (i.e., Ia, Ib and Ic as shown in **Figs. 2a and 3a)**. Exposure ages indicate that the sampled alluvial fans yield ^{10}Be ages of 39.6 ± 1.3 ka, 37.9 ± 1.1 ka and 44.0 ± 3.5 ka and ^{26}Al ages of 36.3 ± 1.6 ka, 30.5 ± 1.4 and 42.2 ± 1.9 ka (for samples MA19-15, 16 and 17, respectively). In the Gramadal area, we collected four

samples, close together, in the alluvial fan surface II as shown in **Figs. 2b and 3b**. The MA19-23 arenitic soil sample and MA19-24 clast sample yield ^{10}Be ages of 59.3 ± 2.0 and 48.9 ± 1.5 ka, and ^{26}Al ages of 41.6 ± 2.3 ka and 48.93 ± 2.5 ka, respectively. The MA19-25 boulder sample shows a ^{10}Be age of 35.1 ± 1.1 ka and a ^{26}Al age of 27.5 ± 2.0 ka. In contrast, the MA19-26 boulder sample shows a ^{10}Be age of 58.4 ± 2.3 ka and a ^{26}Al age of 27.3 ± 2.5 ka.

4.2 Evidence of active contractional deformations along the Amotape front

The TCNs ages presented in the previous sections establish a chronological framework to investigate active tectonic structures along the western edge of the Amotape massif (**Fig 3**). The three-dimensional structural diagram in **Fig. 4a** illustrates the subsurface geometry of the Breita area. Three kilometers north of the Breita area, the Breita River cuts through lower Eocene strata (**Fig. 5a**; see also **Fig. 4a** for location). Espurt et al. (2018) documented the presence of numerous normal and strike-slip faults and few thrusts in the Talara Basin. In the lower Breita River valley, we found several outcrop-scale NW-verging thrusts or imbricate thrust systems deforming the lower Eocene strata (**Fig. 5b**). The main thrusts dip-slip at ~25° to the SE and are associated with conjugate back-thrusts (**Fig. 5b to d**). To determine the trend of the compressional stress, we measured striated fault planes along the Breita River valley at four sites and performed paleo-stress analyses (Angelier, 1990). The paleo-stress diagrams show a NW-trending compression (**Fig. 5a and Supplementary material 1**). This trend is compatible with the NE-trending Amotape massif large-scale structure. The contractional deformation observed along the Breita River valley can be inferred as syn- to post-Eocene, and closely related to the thrust-related uplift of the Amotape massif (Espurt et al., 2018).

Numerous high-quality seismic reflection profiles and wells have been recently acquired in the southeastern edge of the Talara basin up to the Amotape front, south of the Fernandez

River (**Fig. 6**). To constrain the structural architecture of the Amotape thrust front, we used three seismic reflection profiles (XXV-12-2770, XXV-12-2960 and XXV-12-3160) located ahead of the Breita area provided by Perupetro S.A. (**Fig. 6 and Supplementary material 2**). Interpretation of seismic profiles together with field structural and well data suggest the existence of a major deep-seated thrust system at the western edge of the Amotape massif. This thrust system consists of lower hinterland-dipping thrusts involving the Amotape basement and upper NW- and SE-dipping thrusts deforming Eocene strata with structural reliefs (**Fig. 7**). Some faults may correspond to the reactivation of inherited normal to strike-slip faults as observed across the Talara Basin (Espurt et al., 2018). The structural culmination of the Amotape massif can be interpreted as a classic triangle zone of intercutaneous wedge type (Gil and Flinch, 2022) propagating beneath the Talara basin.

Quaternary surface deformation related to the growth of the Amotape triangle zone is well preserved in the Breita area. In this area, TCNs exposure ages indicate that the alluvial fan surfaces yield similar ages of ~39.0 ± 0.3 ka (**Fig. 3a**). This might suggest that prior to deformation, these surfaces were part of the same alluvial fan. Interestingly, field observations indicate that the alluvial fan is possibly offset by a NE-trending scarp (**Fig. 3a**). The swath profile performed across the scarp indicates a vertical offset of 19 m between MA19-15 and MA19-16 samples (**Fig. 4b**). According to contractional structures observed in lower Eocene strata of the lower Breita River valley (**Fig. 5**), the offset affecting the alluvial fan surface I, at the western front of the Amotape massif, could be interpreted as being related to a NW-verging thrust (**Fig. 4**). This thrust, which was active during the late Pleistocene, likely corresponds to the Amotape massif surface front and testifies for active contractional tectonic regime in the northern Peruvian forearc.

4.3 Late Pleistocene contractional slip rate estimate: a first-order range for the Amotape thrust front activity

In the Breita area, a vertical offset has been observed within a late Pleistocene alluvial fan I (**Figs 3a and 4**). This offset was quantified considering the elevations of the displaced alluvial fan surface, inferred from the elevation of two samples (MA19-15 and 16) collected on either side of the Amotape thrust front. Although this vertical offset is observed at a single site (i.e., Breita area), it was measured to be 19 m (**Fig. 4**). We assume that the alluvial fan deposition was abandoned relatively quickly and the surface of the alluvial fan I, which is now an offset surface, has undergone minimal post-depositional modification. While the dip angle of the Amotape thrust front has not been directly constrained by field measurements, we adopt a value of 25° toward the SE, consistent with nearby NW-verging thrust faults in the lower Breita River valley (**Fig. 5**). To account for uncertainties in the fault dip, we apply a ± 10° range to the adopted 25° value in our slip rate calculation. Thus, we estimated a slip rate along the Amotape thrust front by simple trigonometry:

$$Slip\ rate = \frac{\mathrm{H}}{\sin(\alpha)\ \times\ t}$$

with H, the estimated offset of 19 m, α, the dip of the thrust fault plane of 25 ± 10°, and t, the mean minimum exposure age of the alluvial fan of 39.0 ± 0.3 ka. The uncertainty (Δ) of the slip rate is calculated by considering the uncertainties related to the vertical offset (ΔH), the exposure age (Δt) and the dip of the thrust fault plane ($\Delta\alpha$) as follows:

$$\Delta Slip\ rate = \sqrt{\left(\frac{\Delta H}{H}\right)^2 + \left(\frac{\Delta t}{t}\right)^2 + \left(\frac{\Delta \alpha}{\alpha}\right)^2}.$$

We thus calculate an estimated slip rate of 1.15 m/ka ± 0.46 m/ka along the Amotape thrust front (**Fig. 4b**).

5. Discussion

5.1 Chronology and deformation quantification: Interpretations and limits

5.1.1 Age of alluvial fan surfaces

The results of TCN exposure ages from the Breita and Gramadal areas show contrasting patterns. In the following discussion, we will discuss the factors that complicate the interpretation of TCN exposure ages of alluvial fan surfaces and the limitations of TCN dating.

The application of TCN dating methods to alluvial fan surfaces is still under debate. A notable source of uncertainty arises from the influence of as yet unidentified geological and geomorphological processes, which can complicate the interpretation of dating results (Owen et al., 2011; Ivy-Ochs et al., 2013). As demonstrated by Owen et al. (2011), significant uncertainties can be introduced by weathering, exhumation, and the protection of samples by surface materials. These factors often reduce nuclide concentrations, leading to an underestimation of the true age of alluvial fan surfaces. To mitigate these biases, it is recommended that multiple samples be collected from the same surface. When ages are statistically consistent, the surface is likely to be minimally affected by alteration or exhumation. Conversely, dispersed age distributions suggest significant geological processes influencing fan formation, leading to variability in TCN concentrations (Machette et al., 2008; Owen et al., 2011; Ivy-Ochs et al., 2013). Nuclide inheritance occurs when sediments contain pre-existing cosmogenic nuclides prior to deposition (Owen et al., 2011; Schide, 2022). This phenomenon results in elevated nuclide concentrations and consequently overestimated surface ages. Inheritance can occur either before sediment mobilization or during transport. Prolonged transport and slow bedrock erosion in the source area serve to further increase inherited concentrations. The three exposure ages obtained in the Breita area (alluvial fan surfaces Ia, Ib, Ic) are consistent, indicating minimal influence from inheritance (**Fig. 3a and**

Table 1). When considering ^{10}Be concentrations for these three samples, they are statistically indistinguishable, following Ward and Wilson (1978) and their mean value is of 113.3 ± 2.5 at/g which yields an age of 38.6 ± 0.8 ka. Considering the same procedure for ^{26}Al, it appears that the concentration of sample MA19-16 is a potential outlier, while the two other samples MA19-17 and 18 are statistically undistinguishable allowing to determine a mean ^{26}Al concentration of 773.5 ± 24.1 at/g. This mean ^{26}Al concentration yields an age of 38.9 ± 1.7 ka. Therefore, considering these two ages, one can conclude that the alluvial fan surfaces (Ia, Ib, Ic) from the Breita area is exposed since ~39 ka. The results suggest that the surfaces are likely to have been minimally affected by weathering or exhumation processes (**Table 1**). This is probably due to the relatively modest size and moderate slope of the Breita watershed (~16%; **Fig. 8**), which limits sediment recycling, thus reducing the inheritance. Consequently, the sedimentary dynamics in the Breita area appears to be simple, contributing to the preservation of robust exposure ages.

Conversely, the samples of alluvial fan surface II of the Gramadal area show a greater dispersion, which warrant a separate scientific reasoning (**Fig. 3b and Table 1**). For example, the MA19-25 boulder sample gives the youngest age (**Fig. 3b**), whereas the MA19-26 boulder sample shows a different pattern, with much older ^{10}Be age and younger ^{26}Al age (**Fig. 3b**). This significant disparity in ^{26}Al/^{10}Be ratio for MA19-26 boulder sample suggests the presence of inherited nuclides (**Table 1a**). Indeed, the more extensive watershed and the steeper slope (35%; **Fig. 8**) of the Gramadal area result in a higher probability of inherited nuclide concentration, indicating a more complex exposure history. However, due to the absence of modern sediment samples (*i.e.*, zero exposition), direct estimation of inheritance could not be conducted. Therefore, we used a different approach to estimate inheritance. To achieve this, we compared the age distributions of the Breita and Gramadal areas.

Using the *Chi-2* approach pioneered by Ward and Wilson (1978), it revealed that all the ^{10}Be ages within the Breita area were found to be statistically indistinguishable, thereby yielding a mean age of 39.0 ± 0.3 ka (1-sigma standard deviation; **Table 1a**). For ^{26}Al, excluding the outlier MA19-16, the remaining samples yielded a mean age of 39.9 ± 0.4 ka. In contrast, the Gramadal area exhibits greater age dispersion, indicative of a more complex exposure history (**Fig. 3b and Table 1b**). This complexity is evident in the "*banana plot*" (Lal, 1991), which shows the ^{26}Al/^{10}Be ratio versus ^{10}Be concentrations (**Fig. 9**). While MA19-24 appears consistently exposed, other samples fall within the burial area, further highlighting the complexity of the Gramadal area exposure history (**Fig. 9**).

The following factors likely contribute to this complexity:

a/ geological and geomorphological processes affecting these samples in the Gramadal area are complex, and storage and mixing of materials may have influence TCN concentrations (**Fig. 8b**; Owen et al., 2011; Schide, 2022). The samples may have experienced periods of instability resulting in the rolling of boulders and therefore a non-constant exposure history (several parts of the same boulder may have been exposed at different periods regarding their position to incident cosmic ray particles).

b/ in the Gramadal watershed, where the presence of channel logjam indicates a significant accumulation of materials (**Fig. 8a**), the occurrence of past extreme events (e.g., ENSO-type events) may have resulted in the release of stored materials, affecting measured concentrations.

c/ the large Gramadal watershed, with its steeper slopes than the smaller Breita watershed, has accelerated water flow, leading to pronounced incision and higher erosion rates, as evidenced by the presence of the “V”-shaped valley (**Fig. 8a,b**).

d/ time for transporting sediments from the adjacent hillslopes towards alluvial fans is forced by precipitation regimen in alluvial fans, so ages of boulders are going to be different in each alluvial fan (**Fig. 8**).

Despite the multitude of processes likely to influence TCN concentrations, it is reasonable to assume that the Breita and Gramadal alluvial fans have ceased deposition and that their surfaces have been exposed since 39 and 50 ka.

5.1.2 Estimated slip rate

In the Breita area, we present the first quantitative estimate of late Pleistocene slip rate along the Amotape thrust front. At this site, direct measurements of thrust dip were not possible, limiting our ability to precisely constrain the fault geometry. To address this limitation, we adopt a fault dip of 25°, inferred from nearby structural observations in the lower Breita River valley (**Fig. 5**), and account for a ± 10° uncertainty around this value. This relatively broad uncertainty range reflects the possibility that the dip could be as low as 15°, particularly if a low-angle décollement geometry is considered instead of a steeper thrust ramp. This interpretation is corroborated by field observations in the area, where a well-developed triangle zone of the intercutaneous wedge type (**Fig. 5;** Gil and Flinch, 2022) has been documented. Such structures typically form above intermediate to deep décollement levels. Based on a vertical offset of 19 m between MA19-15 and MA19-16 samples and, a mean minimum exposure age of 39.0 ± 0.3 ka (**Fig. 4b**), we estimate a contractional slip rate of 1.15 ± 0.46 m/ka (**Fig. 4b**).

This estimate incorporates uncertainties in both displacement and exposure age, as well as the assumed fault dip, through a consistent and transparent approach to error propagation. As highlighted by Zechar and Frankel (2009), slip rates derived from geomorphic markers must explicitly account for the influence of assumptions, particularly regarding fault geometry and event timing, and are best expressed as ranges or probability distributions rather than

fixed values. Although this estimate is based on a single site, it provides a first-order constraint on late Pleistocene deformation along this segment of the Amotape thrust. It represents a valuable starting point for quantifying recent contractional activity in this under-documented forearc region and underscores the need for additional observations and improved structural data to refine regional slip rate assessments.

5.2 Implications for late Pleistocene geodynamics in the north Peruvian forearc

5.2.1 Seismicity and morphotectonic evidence of active shortening

Seismicity data from the past five decades provide key insights into the ongoing crustal deformation in the north Peruvian forearc. **Fig. 10** shows hypocentres and focal mechanisms data from the ISC catalogue for the period 2000 to 2024 in map and cross-section. The map view of the distribution of the seismicity (**Fig.10a**) shows a cluster of higher seismic activity within the Talara basin and the Amotape massif, where seismic events are concentrated along what is inferred to be the footwall of the Amotape thrust front. This region shows a higher frequency of seismic events compared to adjacent areas, particularly the south-west coastal region (**Fig. 10**). The distribution of the seismicity in cross-section provides strong evidence of intense seismic crustal activity above the E-dipping Nazca slab and across a 100 km-wide zone from the coast (**Fig. 10b**). The spatial distribution of hypocenters indicates that most seismic events are located in the upper crust, particularly between 10 and 20 km depth. Many of these earthquakes exhibit thrust mechanisms that may correspond to active crustal faults beneath the Amotape massif (**Figs. 5 and 10**). The focal mechanisms are consistent with a roughly ~E-W oriented compressive axis, indicating a crustal active compressive regime in the forearc. The ~E–W-trending maximum horizontal stress, as determined by focal mechanisms, is consistent with the contractional structures observed in the Breita River valley (**Figs. 5, 6 and 7**) and the NE-trending escarpment that offsets the alluvial fan surfaces (**Figs. 3a and 4**). This spatial correlation strongly suggests that the western front of the Amotape

massif has remained tectonically active since the late Pleistocene, and is still active at present day.

While the Breita area clearly displays active contractional tectonics regime, the field identification of analogous processes within the Gramadal area is more challenging. In the Gramadal area, outcrop conditions and dense vegetation currently hinder the observation of Quaternary surface deformation and recent front activity of the Amotape massif. Additionally, the challenge of identifying deformation features in the Gramadal area may also reflect a low deformation rate environment, which is further complicated by the intense surface processes at play. However, the prominent structural relief of the Amotape massif in this region suggests that the contractional tectonic regime observed in the Breita area (**Fig. 3b**) likely extends into the Gramadal area. The slightly higher elevation (61 m) of the Gramadal alluvial fan, and its greater incision in comparison with the Breita area, could suggest its tectonic uplift as controlled by an active thrust front located further west in the Talara basin. This hypothesis is further supported by the regional seismicity pattern shown in **Fig. 10**, which includes the two target areas. Further field investigations are required along the lower Gramadal River to precise these structural considerations.

5.2.2 Interseimic deformation and tectonic implications

Building upon these observations, the integration of geological, geomorphological, and geochronological data supports the occurrence of active shortening for at least the last ~40 ka on the northwestern flank of the Amotape massif, located more than 200 km inland from the trench (**Fig. 1**). These new data include (1) the offset of a late Pleistocene alluvial fan surface, combined with TCN surface exposure ages, along the front of the Amotape massif (2) structural data suggesting NW-trending contractional deformation. The newly discovered active thrust in this study may be associated with thin-skin tectonics linked to a shallow décollement. However, previous work by Espurt et al. (2018), proposed that the northern

Peruvian forearc system is primarily dominated by thin-skinned tectonics involving basement deformation (**Fig. 1c**). Our seismic data are consistent with this interpretation, suggesting that the active thrust in this study could be connected to a deep-seated thrust system beneath the Amotape massif (**Figs. 6, 7**). This hypothesis is further supported by the seismicity data, which also indicate deformation involving the basement (**Fig. 10**). Such an architecture aligns with the evolutionary model proposed by Lacombe and Mouthereau (2002), in which tectonic deformation evolves from an initial thin-skinned regime to a combination of both thin- and thick-skinned tectonics. We consider this model particularly well suited to explain the structural evolution observed in our study area. Further field studies in the forearc region may provide more evidence to support our model. Our results suggest that active thrust tectonics may be more widespread in the onshore Peruvian forearc than previously recognized, leading to significant active crustal deformation and shortening related to ongoing subduction.

Our study area is the northernmost part of a 1000 km-long subduction segment that has been characterized with a low interseismic coupling models based on GNSS-derived velocity fields (Chlieh et al., 2014; Nocquet et al., 2014; Villegas-Lanza et al., 2016; Jarrin et al., 2023). This low interseismic coupling implies creep along the plate interface and weak crustal deformation. However, we provided evidence for late Pleistocene permanent crustal deformation in the northern Peruvian forearc, including the offset of an alluvial fan surface by a thrust fault, that is associated with a significant crustal seismic activity. The permanent deformation distribution along the study area also includes a major Quaternary coastal uplift testified by the uplift of marine terraces (Bourgois et al., 2006; Pedoja et al., 2006), as in southern Peru and Chile (Saillard et al., 2009, 2011, 2017). Although the forearc region is characterized by a weak interseismic coupling, active deformation occurs within the forearc prism, in particular through ongoing active shortening and coastal uplift. This particular state of stress is perhaps due to the regional tectonic context of the study area, which lies at the

hinge between the opening of the Gulf of Guayaquil and the tectonic escape of the Inca sliver (**Fig. 1a**). The area represents a major structural and kinematic bloc, accommodating deformation between adjacent crustal blocks (Jarrin et al., 2023). A comprehensive understanding and quantification of permanent deformation in this region are therefore essential to better understand the underlying tectonic mechanisms and their implications. Moreover, incorporating the long-term deformation into the calculation of interseismic coupling models is a major step to further improve the seismic hazard assessment.

6. Conclusions

In this study, we propose a new structural interpretation for the onshore northern Peruvian forearc system, which includes the first TCNs dating of alluvial fans, together with surface and subsurface structural data along the front of the Amotape structural high. Our results set out a model for the long-term evolution of a forearc system located in a region that has been characterized by limited active tectonics, yet exhibiting active shortening, at least for the last ~40 ka. Morphotectonics analysis indicates the presence of an active thrust that reaches the surface and offsets an alluvial fan. It is possible that this active thrust is connected to a deep-seated thrust system in the crustal basement of the Peruvian forearc. We provide the first evidence of Amotape thrust front activity since late Pleistocene (~40 ka), related to the uplift of the crustal-scale Amotape massif thrust system. The slip rate along the Amotape thrust is estimated at 1.15 ± 0.46 m/ka, since ~40 ka. Although the zone has been characterized by a weak interseismic coupling on the subduction interface, active forearc deformation, in particular shortening, occurs along a crustal thrust reaching the surface, 200 km from the trench.

Acknowledgments

This work is part of the A. Peuzin's PhD thesis (EDSFA 284) and supported by the ANR MARACAS (ANR-18-CE31-0022; PI: M. Saillard). G. Aumaître, F. Zaidi and K.

Keddadouche are thanked for their valuable assistance during ^{10}Be and ^{26}Al measurements at the ASTER AMS national facility (CEREGE, Aix-en-Provence) which is supported by the INSU/CNRS, IRD and member of Aix-Marseille Platform and REGEF networks. We also thank PERUPETRO S.A. for providing the subsurface data. Seismic profiles were interpreted using the MOVE Software Suite donated by PE Limited. We would like to thank the representatives of the IRD in Peru and Ecuador for their support. Finally, we thank Patrice Baby and Stéphane Brusset for their contribution to the first field exploration in this area in 2013. We also thank P. Marques Figueiredo and two anonymous reviewers and, Editor Prof. Gideon Rosenbaum for their constructive comments that allowed us to improve the manuscript and the figures in many points.

References

Angelier, J., 1990. Inversion of field data in fault tectonics to obtain the regional stress - III. A new rapid direct inversion method by analytical means. Geophysical Journal International, 103(2), 363-376.

Angelier, J., 1984. Tectonic analysis of fault slip data sets. Journal of Geophysical Research: Solid Earth, 89(B7), 5835-5848.

Auguy, C., Calvès, G., Calderon, Y., Brusset, S., 2017. Seismic evidence of gas hydrates, multiple BSRs and fluid flow offshore Tumbes Basin, Peru. Marine Geophysical Research, 38, 409–423. https://doi.org/10.1007/s11001-017-9319-2

Arnold, M., Merchel, S., Bourlès, D. L., Braucher, R., Benedetti, L., Finkel, R. C., Klein, M. 2010. The French accelerator mass spectrometry facility ASTER: improved performance and developments. Nuclear Instruments and Methods in Physics Research Section B: Beam Interactions with Materials and Atoms, 268(11-12), 1954-1959.

Avouac, J. P., 1993. Analysis of scarp profiles: evaluation of errors in morphologic dating. Journal of Geophysical Research: Solid Earth, 98(B4), 6745-6754.

Balco, G., Soreghan, G. S., Sweet, D. E., Marra, K. R., Bierman, P. R. 2013. Cosmogenic-nuclide burial ages for Pleistocene sedimentary fill in Unaweep Canyon, Colorado, USA. Quaternary Geochronology, 18, 149-157.

Beauval, C., Yepes, H., Palacios, P., Segovia, M., Alvarado, A., Font, Y., Aguilar, J., Troncoso, L., Vaca, S., 2013. An Earthquake Catalog for Seismic Hazard Assessment in Ecuador. Bulletin of the Seismological Society of America, 103, 773–786. https://doi.org/10.1785/0120120270

Benedetti, L., Manighetti, I., Gaudemer, Y., Finkel, R., Malavieille, J., Pou, K., & Keddadouche, K. 2013. Earthquake synchrony and clustering on Fucino faults (Central Italy) as revealed from in situ 36Cl exposure dating. Journal of Geophysical Research: Solid Earth, 118(9), 4948-4974.

Benedetti, L., Van der Woerd, J. 2014. Cosmogenic nuclide dating of earthquakes, faults, and toppled blocks. Elements, 10(5), 357–361.

Bevis, M., Kendrick, E., Smalley Jr, R., Brooks, B., Allmendinger, R., Isacks, B., 2001. On the strength of interplate coupling and the rate of back arc convergence in the central Andes: An analysis of the interseismic velocity field. Geochemistry, Geophysics, Geosystems, 2(11).

Bosworth, T. O., 1922. Geology of the Tertiary and Quaternary periods in the northwest part of Peru. London, UK: Macmillan and Company, 434 p.

Braucher, R., Merchel, S., Borgomano, J., Bourlès, D. L., 2011. Production of cosmogenic radionuclides at great depth: A multi element approach. Earth and Planetary Science Letters, 309(1-2), 1-9.

Braucher, R., Guillou, V., Bourlès, D. L., Arnold, M., Aumaître, G., Keddadouche, K., Nottoli, E. 2015. Preparation of ASTER in-house 10Be/9Be standard solutions. Nuclear Instruments and Methods in Physics Research Section B: Beam Interactions with Materials and Atoms, 361, 335-340.

Brooks, B. A., Bevis, M., Smalley Jr, R., Kendrick, E., Manceda, R., Lauria, E., Araujo, M., 2003. Crustal motion in the Southern Andes (26°–36° S): Do the Andes behave like a microplate? Geochemistry, Geophysics, Geosystems, 4(10).

Burbank, D. W., Anderson, R. S., 2011. Tectonic geomorphology. John Wiley & Sons: 198-200.

Calvès, G., Auguy, C., de Lavaissière, L., Brusset, S., Calderon, Y., Baby, P., 2017. Fore-arc seafloor unconformities and geology: Insight from 3-D seismic geomorphology analysis, Peru. Geochemistry, Geophysics, Geosystems, 18, 3062–3077. https://doi.org/10.1002/2017GC007036

Chlieh, M., Mothes, P.A., Nocquet, J.-M., Jarrin, P., Charvis, P., Cisneros, D., Font, Y., Collot, J.-Y., Villegas-Lanza, J.-C., Rolandone, F., Vallée, M., Regnier, M., Segovia, M., Martin, X., Yepes, H., 2014. Distribution of discrete seismic asperities and aseismic slip along the Ecuadorian megathrust. Earth and Planetary Science Letters, 400, 292–301.

Chmeleff, J., von Blanckenburg, F., Kossert, K., Jakob, D., 2010. Determination of the 10Be half-life by multicollector ICP-MS and liquid scintillation counting. Nucl. Instruments Methods Phys. Res. Sect. B Beam Interact. With Mater. Atoms, 268, 192–199.

Cobos, L., 2010. Estudio Ontegrado del Golfo de Guayaquil del Mioceno al Reciente. Ph.D tesis, Facultad de Ingeniera en Ciencas de la Tierra, Guayaquil – Ecuador, 172 p.

Collot, J.-Y., Charvis, P., Gutscher, M.-A., Operto, E. 2002. Exploring the Ecuador-Colombia active margin and inter-plate seismogenic zone. Eos, Transactions American Geophysical Union, 83(17), 185–190, https://doi.org/10.1029/2002EO000120

Clift, P. D., Pecher, I., Kukowski, N., Hampel, A. 2003. Tectonic erosion of the Peruvian forearc, Lima Basin, by subduction and Nazca Ridge collision. Tectonics, 22(3), 1023. https://doi.org/10.1029/2002TC001386.

David, B., Thomas, J., 2008. Handbook of Landscape Archaeology (1st ed.). Routledge. 720 p, https://doi.org/10.4324/9781315427737

DeVries, T. J., 1986. The geology and paleontology of the tablazos in northwest Peru, Ph.D. dissertation, 964 pp., Ohio State Univ., Columbus, Aug.

Dunai, T. J., 2010. Cosmogenic nuclides: principles, concepts and applications in the earth surface sciences. Cambridge University Press.

Echevin, V., Colas, F., Espinoza-Morriberon, D., Vasquez, L., Anculle, T., Gutierrez, D., 2018. Forcings and evolution of the 2017 coastal El Niño off northern Peru and Ecuador. Frontiers in Marine Science, 5, 367.

Espurt, N., Brusset, S., Baby, P., Henry, P., Vega, M., Calderon, Y., Saillard, M., 2018. Deciphering the Late Cretaceous-Cenozoic structural evolution of the North Peruvian forearc system. Tectonics, 37(1), 251-282.

Fernández, J., Martínez, E., Calderón, Y., Hermoza, W., Galdos, C., 2005. Tumbes and

Talara basins hydrocarbon evaluation. Perupetro S.A., Basin Evaluations Group Exploration Department. pp. 130, internal report. Retrieved from www.perupetro.com.pe

Fildani, A., Hessler, A. M., Graham, S. A., 2008. Trench-forearc interactions reflected in the sedimentary fill of Talara basin, northwest Peru. Basin Research, 20(3), 305-331.

Gil, W., Flinch, J. F. 2022. Several types of triangle zones from the Subandean ranges of Peru: Fish-tails, tectonic wedges and passive-roof duplexes. Marine and Petroleum Geology, 146, 105968.

Gillespie, A., and Molnar, P., 1995. Asynchronous maximum advances of mountain and continental glaciers. Reviews of Geophysics, 33(3), 311-364.

Gosse, J. C., and Phillips, F. M., 2001. Terrestrial in situ cosmogenic nuclides: theory and application. Quaternary Science Reviews, 20(14), 1475-1560.

Harvey, A. M., Silva, P. G., Mather, A. E., Goy, J. L., Stokes, M., Zazo, C. 1999. The impact of Quaternary sea-level and climatic change on coastal alluvial fans in the Cabo de Gata ranges, southeast Spain. Geomorphology, 28(1-2), 1-22.

Hayes, G. P., Moore, G. L., Portner, D. E., Hearne, M., Flamme, H., Furtney, M., Smoczyk, G. M., 2018. Slab2, a comprehensive subduction zone geometry model. Science, 362(6410), 58-61.

Heermance, R. V., Chen, J., Burbank, D. W., Miao, J., 2008. Temporal constraints and pulsed Late Cenozoic deformation during the structural disruption of the active Kashi foreland, northwest China. Tectonics, 27(6).

Hedrick, K., Owen, L. A., Rockwell, T. K., Meigs, A., Costa, C., Caffee, M. W., & Ahumada, E. 2013. Timing and nature of alluvial fan and strath terrace formation in the Eastern Precordillera of Argentina. Quaternary Science Reviews, 80, 143-168.

Heisinger, B., Lal, D., Jull, A.J.T., Kubik, P., Ivy-Ochs, S., Knie, K., Nolte, E., 2002b. Production of selected cosmogenic radionuclides by muons; 2. Capture of negative muons. Earth Planet. Sci. Lett. 200, 357–369.

Higley, D.K., 2004. The Talara Basin Province of Northwestern Peru, Cretaceous-Tertiary Total Petroleum System. US Department of the Interior, US Geological Survey.

Hoffmann-Rothe, A., Kukowski, N., Dresen, G., Echtler, H., Oncken, O., Klotz, J., and Kellner, A. 2006. Oblique convergence along the Chilean margin: partitioning, margin-parallel faulting and force interaction at the plate interface. The Andes: Active Subduction Orogeny, 125-146.

Ivy-Ochs, S., Dühnforth, M., Densmore, A. L., Alfimov, V., 2013. Dating fan deposits with cosmogenic nuclides. Dating Torrential Processes on Fans and Cones: Methods and Their Application for Hazard and Risk Assessment, 243-263.

Jara-Muñoz, J., Melnick, D., Strecker, M. R., 2016. TerraceM: A MATLAB® tool to analyze marine and lacustrine terraces using high-resolution topography. Geosphere, 12(1), 176-195.

Jarrin, P., Nocquet, J. M., Rolandone, F., Audin, L., Mora-Páez, H., Alvarado, A., Cisneros, D., 2023. Continental block motion in the Northern Andes from GPS measurements. Geophysical Journal International, 235(2), 1434-1464.

Keefer, D. K., Moseley, M. E., Defrance, S. D., 2003. A 38 000-year record of floods and debris flows in the Ilo region of southern Peru and its relation to El Niño events and great earthquakes. Palaeogeography, Palaeoclimatology, Palaeoecology, 194(1-3), 41-77.

Kim, K. J., and Sutherland, R., 2004. Uplift rate and landscape development in southwest Fiordland, New Zealand, determined using 10Be and 26Al exposure dating of marine terraces. Geochimica et Cosmochimica Acta, 68(10), 2313-2319.

Korschinek, G., Bergmaier, A., Faestermann, T., Gerstmann, U.C., Knie, K., Rugel, G., Wallner, A., Dillmann, I., Dollinger, G., von Gostomski, C.L., Kossert, K., Maiti, M., Poutivtsev, M., Remmert, A., 2010. A new value for the half-life of 10Be by Heavy-Ion

Elastic Recoil Detection and liquid scintillation counting. Nucl. Instruments Methods Phys. Res. Sect. B Beam Interact. With Mater. Atoms 268, 187–191.
Lal, D., 1991. Cosmic ray labeling of erosion surfaces: in situ nuclide production rates and erosion models. Earth and Planetary Science Letters, 104(2-4), 424-439.
Machette, M. N., Slate, J. L., Phillips, F. M., 2008. Terrestrial cosmogenic-nuclide dating of alluvial fans in Death Valley, California. Geological Survey (US).
Merchel, S., Herpers, U., 1999. An update on radiochemical separation techniques for the determination of long-lived radionuclides via accelerator mass spectrometry, Radiochim. Acta 84. 215–219.
Merchel, S., Bremser, W., 2004. First international 26Al interlaboratory comparison – Part I. Nucl. Instruments Methods Phys. Res. Sect. B Beam Interact. With Mater. Atoms 223–224, 393–400.
Merchel, S., Arnold, M., Aumaître, G., Benedetti, L., Bourlès, D.L., Braucher, R., Alfimov, V., Freeman, S.P.H.T., Steier, P., Wallner, A., 2008. Towards more precise 10Be and 36Cl data from measurements at the 10–14 level: influence of sample preparation, Nucl. Instr. Meth. B, 266, 4921–4926.
Nocquet, J.-M., Villegas-Lanza, J.C., Chlieh, M., Mothes, P.A., Rolandone, F., Jarrin, P., Cisneros, D., Alvarado, A., Audin, L., Bondoux, F., Martin, X., Font, Y., Régnier, M., Vallée, M., Tran, T., 2014. Motion of continental slivers and creeping subduction in the northern Andes. Nature Geoscience, 7(4), 287-291.
Ortlieb, L, and Macharé, J., 1993. Former El Niño events: records from western South America, Global and Planetary Change, 7, 181–202.
Pang, L., Lu, H., Wu, D., Guan, X., Zhao, J., Zheng, X., Li, Y., 2021. Late Pleistocene uniform rate of thrusting along the fault's strike: A case study from the northern Tian Shan foreland. Tectonics, 40(4), e2021TC006726.
Owen, L. A., Frankel, K. L., Knott, J. R., Reynhout, S., Finkel, R. C., Dolan, J. F., Lee, J. 2011. Beryllium-10 terrestrial cosmogenic nuclide surface exposure dating of Quaternary landforms in Death Valley. Geomorphology, 125(4), 541-557.
Pardo-Casas, F., Molnar, P., 1987. Relative motion of the Nazca (Farallon) and South American plates since Late Cretaceous time. Tectonics, 6(3), 233-248.
Pedoja, K., Ortlieb, L., Dumont, J. F., Lamothe, M., Ghaleb, B., Auclair, M., Labrousse, B., 2006. Quaternary coastal uplift along the Talara Arc (Ecuador, Northern Peru) from new marine terrace data. Marine Geology, 228(1-4), 73-91.
Peuzin, A., Saillard, M., Espurt, N., Michaud, F., Bulois, C., Praeg, D., Calderon, Y., 2023. Gravity-driven large-scale deformation system in the Tumbes-Guayaquil forearc basin, Northern Andes (Northern Peru-Southern Ecuador). Journal of Structural Geology, 104909.
Quigley, M. C., Sandiford, M., Cupper, M. L., 2007. Distinguishing tectonic from climatic controls on range-front sedimentation. Basin Research, 19(4), 491-505.
Saillard, M., Hall, S. R., Audin, L., Farber, D. L., Hérail, G., Martinod, J., Bondoux, F., 2009. Non-steady long-term uplift rates and Pleistocene marine terrace development along the Andean margin of Chile (31 S) inferred from 10Be dating. Earth and Planetary Science Letters, 277(1-2), 50-63.
Saillard, M., Hall, S. R., Audin, L., Farber, D. L., Regard, V., Hérail, G., 2011. Andean coastal uplift and active tectonics in southern Peru: 10Be surface exposure dating of differentially uplifted marine terrace sequences (San Juan de Marcona, ~ 15.4 S). Geomorphology, 128(3-4), 178-190.
Saillard, M., Audin, L., Rousset, B., Avouac, J. P., Chlieh, M., Hall, S. R., Farber, D. L., 2017. From the seismic cycle to long-term deformation: Linking seismic coupling and Quaternary coastal geomorphology along the Andean megathrust. Tectonics, 36(2), 241-256.
Samworth, E.A., Warburton, E.K., Engelbertink, G.A.P., 1972. Beta Decay of the 26Al

Ground State. Phys. Rev., C5, 138–142.
Sanabria, J., Bourrel, L., Dewitte, B., Frappart, F., Rau, P., Solis, O., Labat, D., 2018. Rainfall along the coast of Peru during strong El Niño events. International Journal of Climatology, 38(4), 1737-1747.
Schide, K. H. (2022). Systematics of cosmogenic nuclide signals following extreme events in the Nepalese Himalaya, Ph.D Thesis, ETH Zurich, 95 p.
Schide, K., Gallen, S. F., Lupker, M. (2022). Modelling the systematics of cosmogenic nuclide signals in fluvial sediments following extreme events. Earth Surface Processes and Landforms, 47(9), 2325-2340.
Séranne, M., 1987. Evolution tectono-sédimentaire du bassin de Talara (nord-ouest du Pérou). Bulletin de l'Institut Français d'Études Andines, 16(3), 103-125.
Siame, L., Bellier, O., Braucher, R., Sébrier, M., Cushing, M., Bourlès, D., Yiou, F., 2004. Local erosion rates versus active tectonics: cosmic ray exposure modelling in Provence (south-east France). Earth and Planetary Science Letters, 220(3-4), 345-364.
Stone, J. O., 2000. Air pressure and cosmogenic isotope production. Journal of Geophysical Research: Solid Earth, 105(B10), 23753-23759.
Tapponnier, P., Ryerson, F. J., Van der Woerd, J., Mériaux, A. S., Lasserre, C. 2001. Long -term slip rates and characteristic slip: keys to active fault behaviour and earthquake hazard. Comptes Rendus de l'Académie des Sciences-Series IIA-Earth and Planetary Science, 333(9), 483-494.
Tavera, H., Vilca, R., Marín, G., 2006. Inferences on the geometry of the Nazca plate in northwestern Perú based on data collected by a local seismograph network. Earth Sciences Research Journal, 10(1), 15-24.
Vega, M., 2009. Architecture tectonique et stratigraphique du bassin d'avant-arc de Tumbes (Nord Pérou) : Implications pour l'exploration des hydrocarbures. Ph.d. Thesis, University of Toulouse III-Paul Sabatier, 191 p.
Villegas-Lanza, J.C., Chlieh, M., Cavalié, O., Tavera, H., Baby, P., Chire-Chira, J., Nocquet, J.-M., 2016. Active tectonics of Peru: Heterogeneous interseismic coupling along the Nazca megathrust, rigid motion of the Peruvian Sliver, and Subandean shortening accommodation: Active Tectonics of Peru. Journal of Geophysical Research Solid Earth, 121, 7371–7394. https://doi.org/10.1002/2016JB013080
Veloza, G., Styron, R., Taylor, M., Mora, A., 2012. Open-source archive of active faults for northwest South America. GSA Today, 22(10), 4-10.
Vuille, M., Bradley, R.S., Keimig F., 2000. Climate Variability in the Andes of Ecuador and Its Relation to Tropical Pacific and Atlantic Sea Surface Temperature Anomalies. J. Climate, 13, 2520–2535.
Ward, G. K., Wilson, S. R., 1978. Procedures for comparing and combining radiocarbon age determinations: a critique. Archaeometry, 20(1), 19-31.
Weber, J. C., Dixon, T. H., DeMets, C., Ambeh, W. B., Jansma, P., Mattioli, G., Pérez, O., 2001. GPS estimate of relative motion between the Caribbean and South American plates, and geologic implications for Trinidad and Venezuela. Geology, 29(1), 75-78.
Wells, L.E., 1987. An alluvial record of El Niño events from northern coastal Peru. J. Geophys. Res., 92(C13), 14463–14470, 10.1029/JC092iC13p14463.
Witt, C., Bourgois, J., 2010. Forearc basin formation in the tectonic wake of a collision-driven, coastwise migrating crustal block: The example of the North Andean block and the extensional Gulf of Guayaquil-Tumbes Basin (Ecuador-Peru border area). Geological Society of America Bulletin, 122, 89–108. https://doi.org/10.1130/B26386.1.

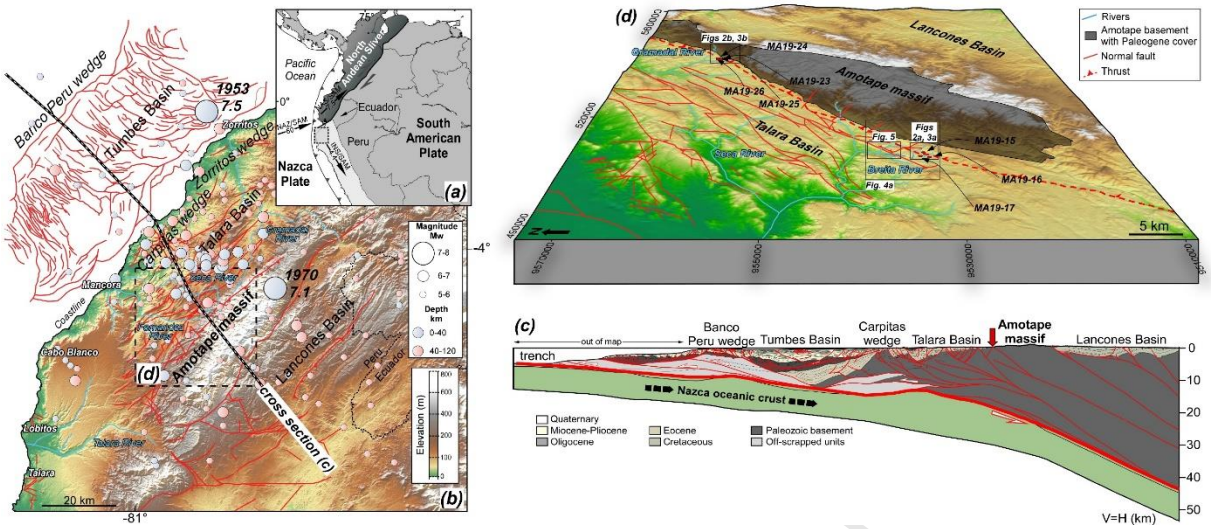

Fig. 1. Geodynamic and structural settings of the north Peruvian forearc system. (a) Geodynamic map of the Central-North Andean active margin related to the Nazca-South American convergence plate system. The dashed black square indicates the location of the study area. The black arrows with numbers indicate the relative convergence rate (in mm/a) and the oblique convergence trend between the Nazca (NAZ) and South American (SAM) Plates and the relative motions of the North Andean Sliver (NAS) and the Inca Sliver (INS) in mm/a (from Villegas-Lanza et al., 2016). (b) Structural map of the north Peruvian forearc system. The dashed black square indicates the location of the Amotape massif region. Crustal seismicity is shown. Epicenters are from the unified earthquakes catalog (1587-2009), displaying magnitude 7 and above (from Beauval et al., 2013). Faults are derived from Espurt et al. (2018). (c) Structural cross-section of the north Peruvian forearc system (see location on b; modified after Espurt et al. (2018)). (d) Three-dimensional structural view of the Amotape massif region. Red dotted line indicates the inferred northwestern Amotape massif thrust front. Coordinate system is UTM zone 17S.

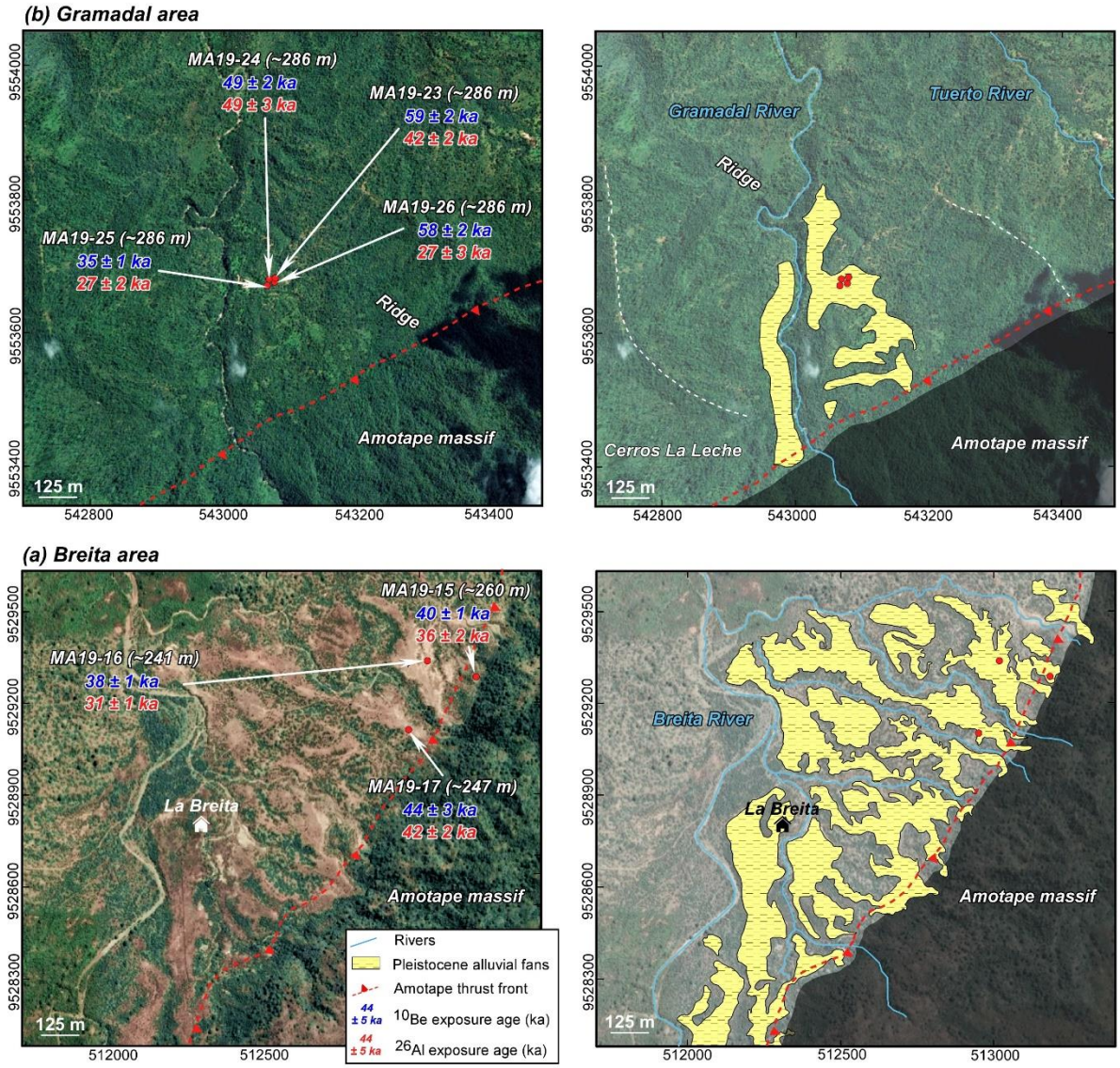

Fig. 2. Mapping of the Quaternary alluvial fan deposits along the Amotape massif front in the Breita (a) and the Gramadal (b) areas on Satellite images from Google Earth. Red circles indicate sample locations with name and altitude. For location, see **Fig. 1d**.

Fig. 3. Geomorphologic field observations along the Amotape thrust front. (a) Panoramic view of the alluvial fan Ia, b and c in the Breita area and the surface offset associated with the Amotape thrust fault. The dashed red line represents the fault trace. (b) Panoramic view of the Gramada area with the abandoned boulders on the surface of the alluvial fan II. ^{10}Be exposure ages are in blue and ^{26}Al exposure ages are in red.

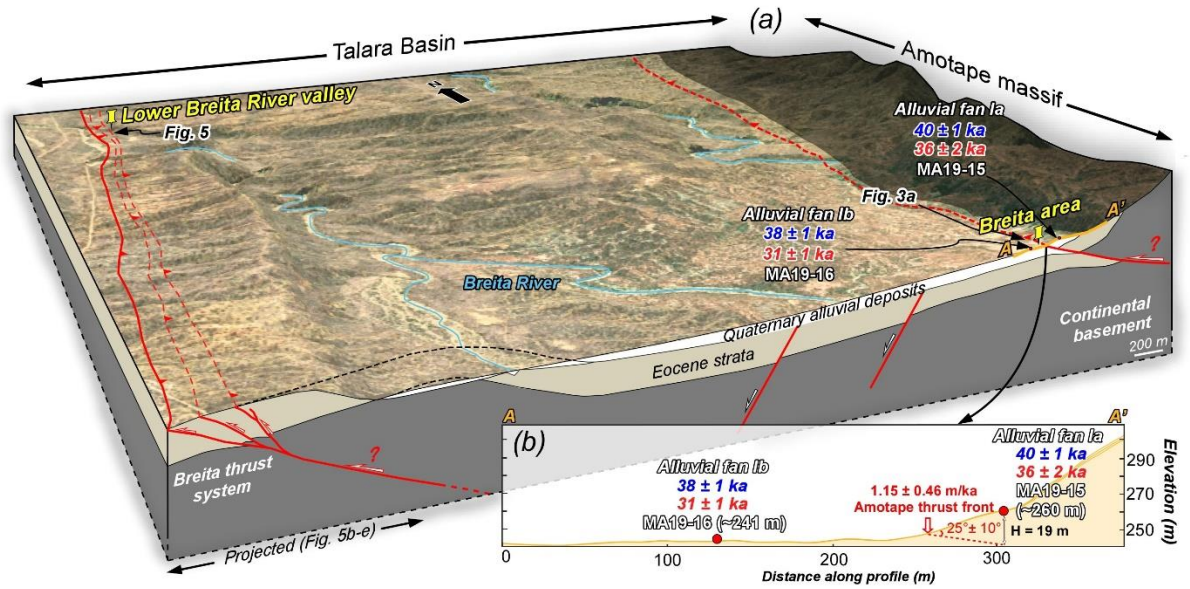

Fig. 4. (a) Three-dimensional structural diagram illustrating the thrust tectonics at the boundary between the Talara Basin and the Amotape massif (Breita area). (b) Swath profile over the Ia and b surfaces and the associated vertical offset H between the two samples. The location of the swath profile is represented in blue on the three-dimensional structural diagram. ^{10}Be exposure ages are in blue and ^{26}Al exposure ages are in red. See text for further explanations.

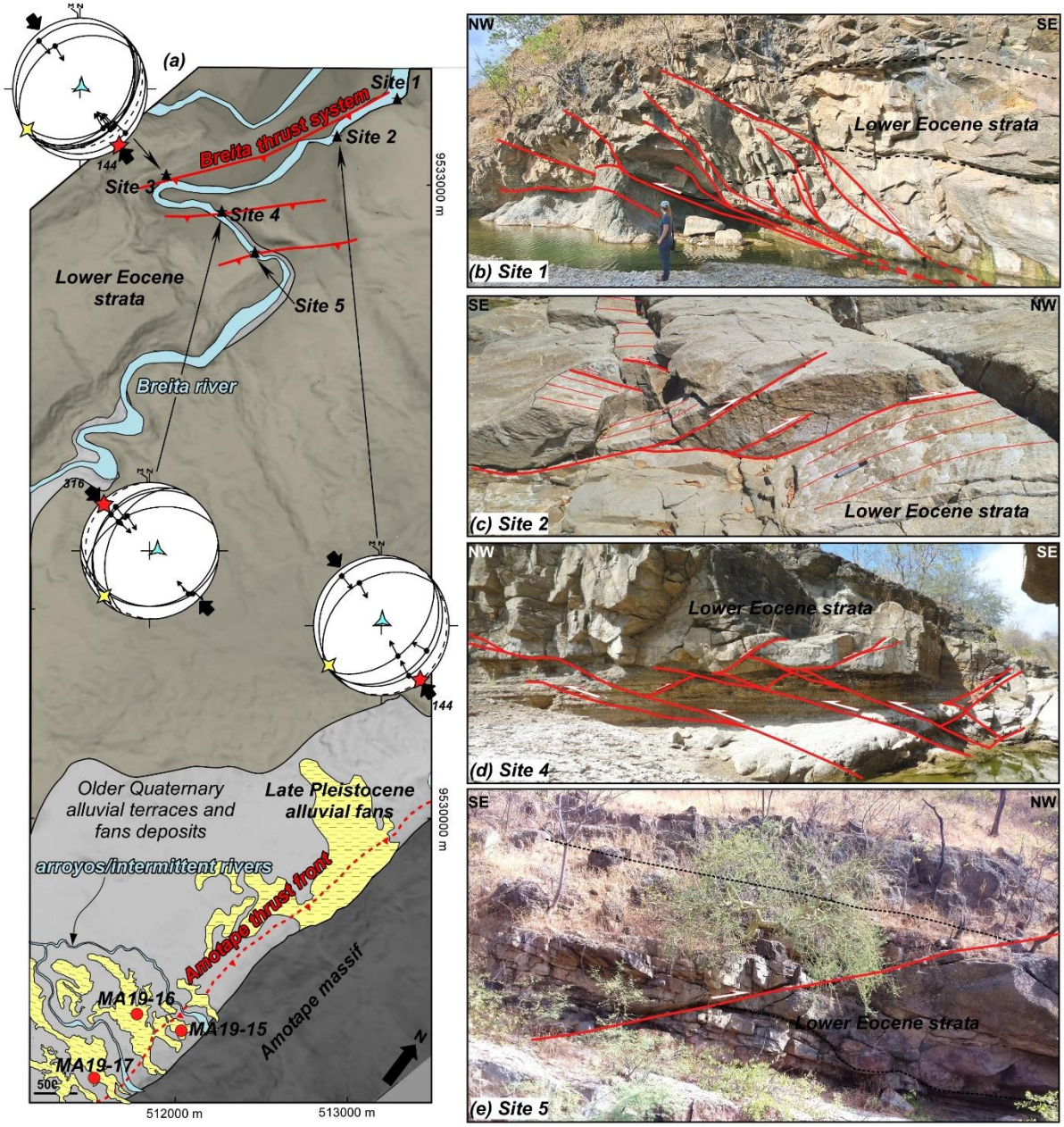

Fig 5. Field evidences for NW-trending compression in lower Eocene strata along the lower Breita River valley. (a) Map of sites with thrust deformation. The compressional structures correspond to reverse faults, imbrications and thrust wedges (b, c, d, e). The paleo-stress reconstruction was performed using the Angelier method (INVD method, Angelier (1990)). Fault slip data are projected in an equal area diagram, lower hemisphere. Principal stress axes (σ1, σ2, and σ3) are symbolized by red five-branch, yellow four-branch, and blue three-branch stars, respectively. Trend of σ1 is indicated by black arrows. The dashed line corresponds to the projection of the bedding dip of lower Eocene strata in the diagram.

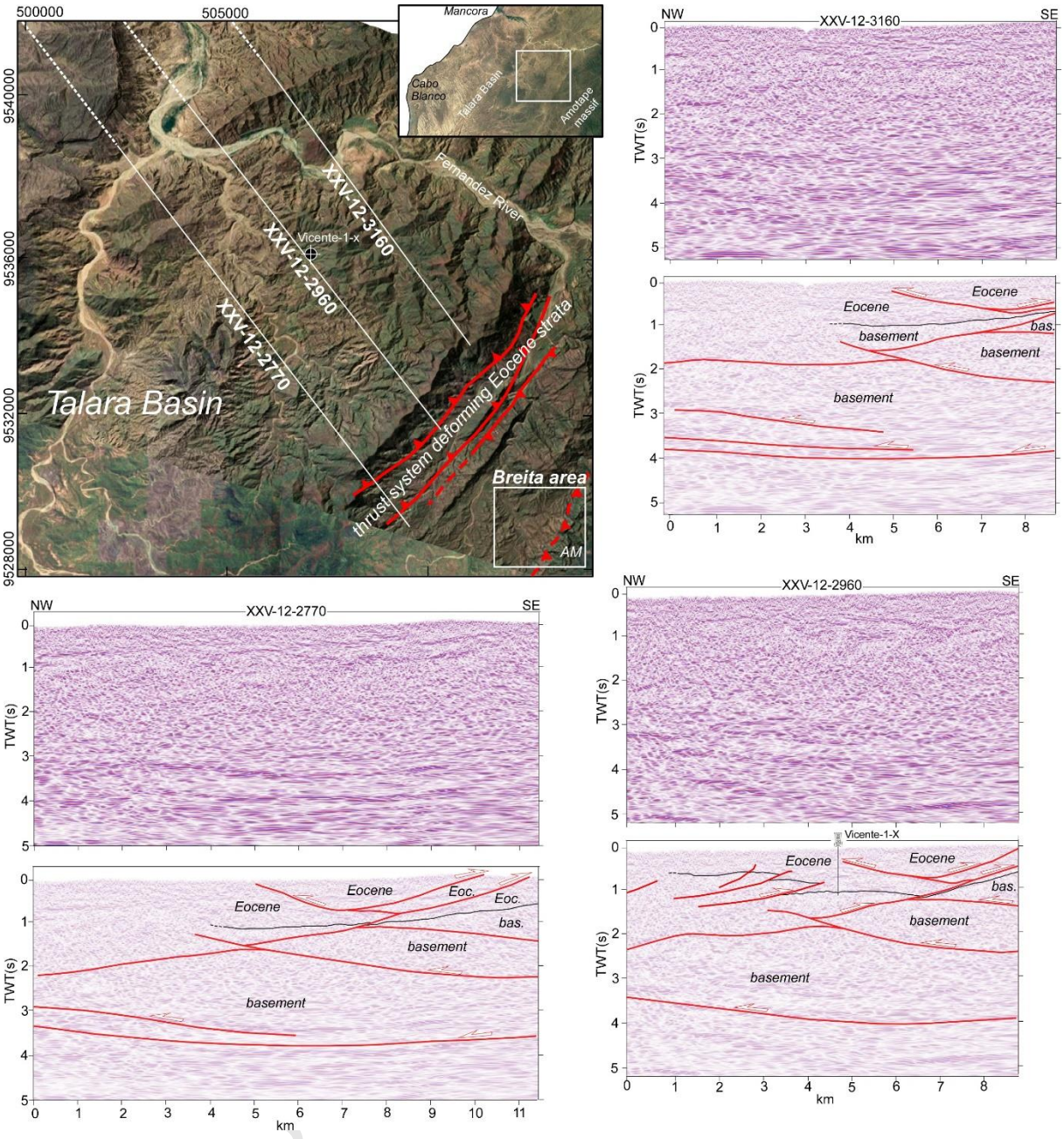

Fig 6. Structural interpretation of subsurface data at the front of the Breita area. Location of the three seismic profiles (white lines with labels) and the Vicente-1-x exploration well (reaching the Amotape basement) available to the northwest of the Breita area (white square). The basemap is from Google Earth ©. The interpretation of subsurface data suggests a classic triangle zone of intercutaneous wedge type (Gil and Flinch, 2022) propagating beneath the southeastern edge of the Talara Basin. The seismic profiles are in second two-way travel time (TWT(s)). AM: Amotape massif.

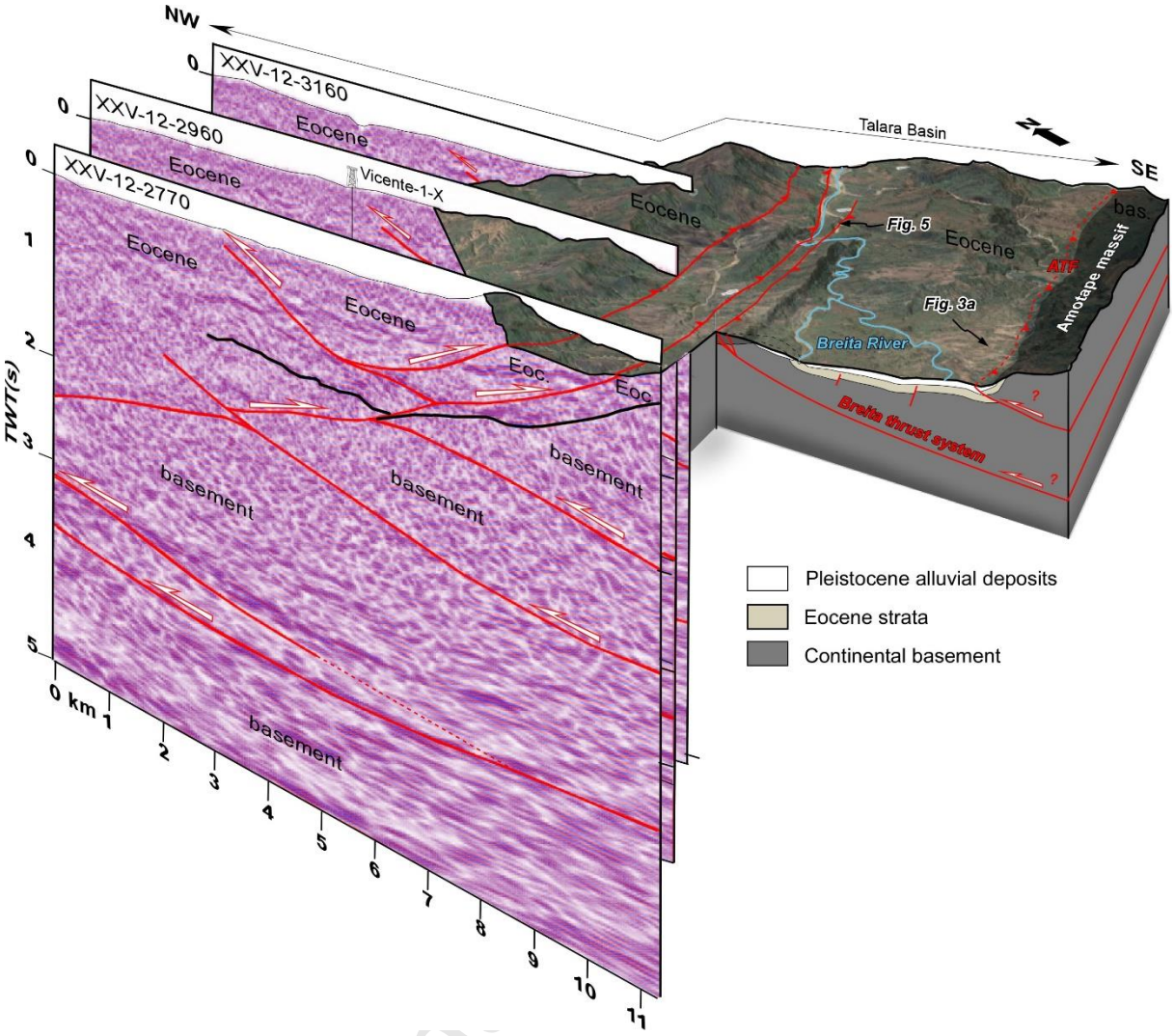

Fig. 7. Three-dimensional view of the subsurface data to the northwest of the Breita area. The seismic profiles are interpreted from field surface and well data (Vicente-1-x). The profiles are in second two-way travel time (TWT(s)). ATF: Amotape thrust front. See text for further explanations.

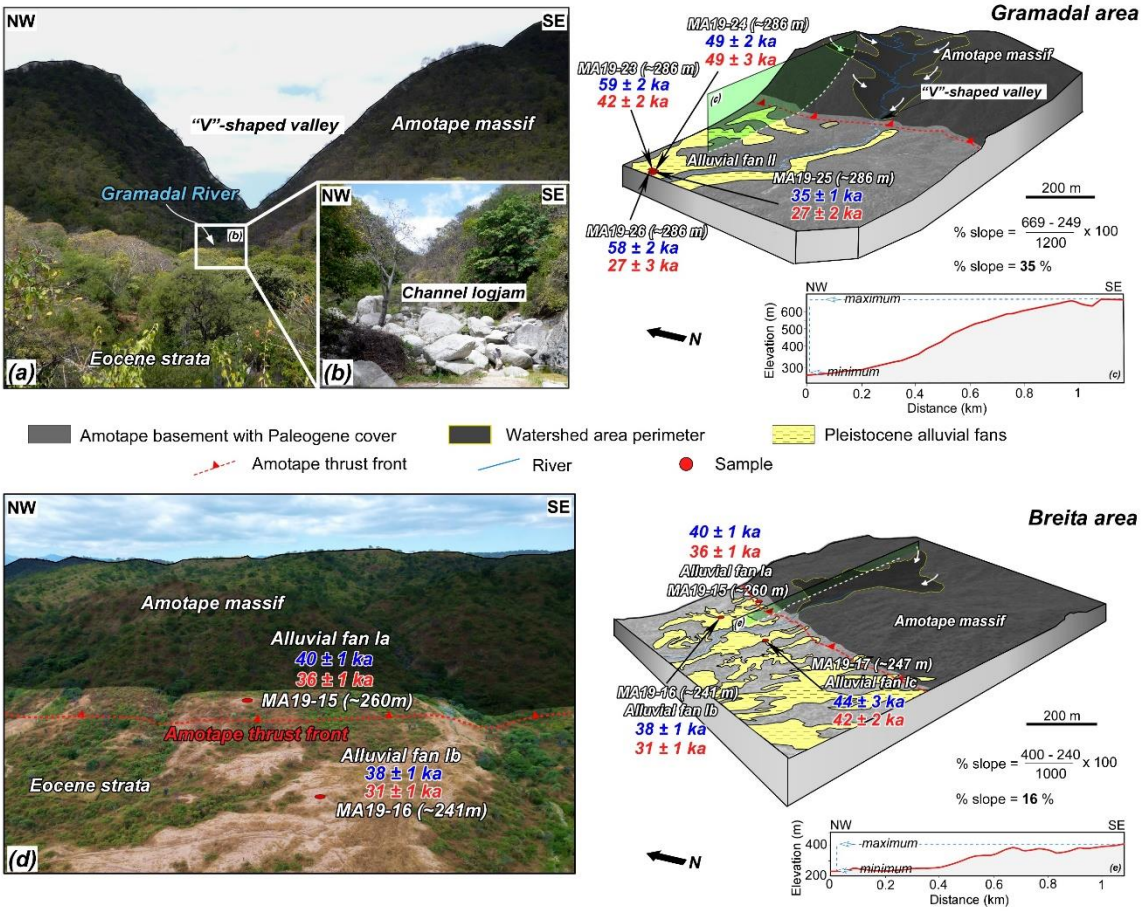

Fig. 8. Geomorphologic field observations in the Gramadal and the Breita areas. (a) Photography showing the "V"-shaped valley in the Gramadal area. (b) Photography of a substantial channel logjam that illustrates the processes of material storage and mixing in the Gramadal River (for location, see **Fig. 4a**). (c) Three-dimensional block diagram of the Gramadal area illustrating the watershed area perimeter and the distance between the sampled alluvial fans and their source origin. AUV photography (d) and three-dimensional block diagram (e) of the Breita area. The topographic profiles (c') and (e') show the average slope between the maximum and minimum elevations of the areas. ^{10}Be and ^{26}Al exposure ages are indicated in blue and in red, respectively.

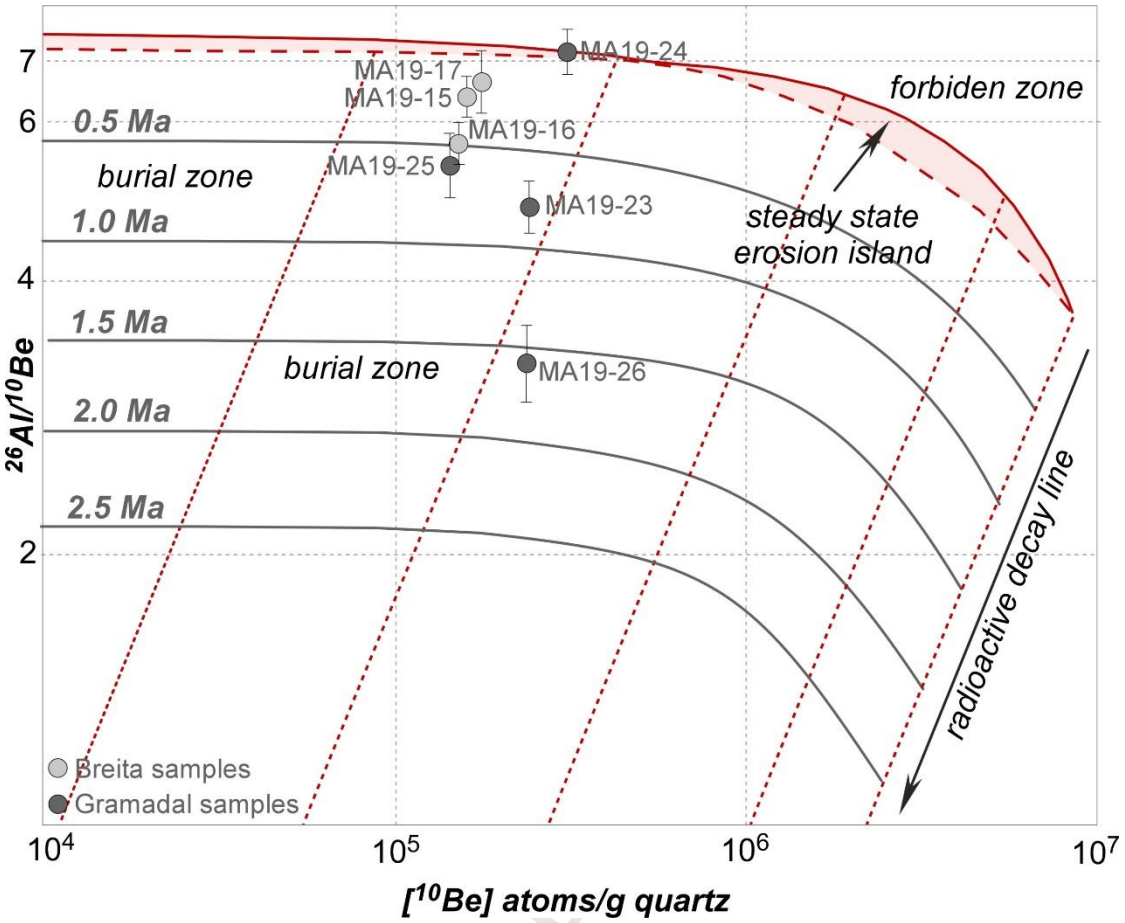

Fig. 9. Banana plot (Lal, 1991) for ^{10}Be and ^{26}Al ages of samples collected in Breita and Gramadal areas. Note that the ^{10}Be and ^{26}Al ages for MA19-15, 16, 17 and 24 sample are indistinguishable and the ^{26}Al/^{10}Be ratios for all samples overlap (within the one-sigma uncertainty) the constant-exposure production-rate ratio line. This indicates that the samples do not have complex exposure histories detectable by the ^{26}Al/^{10}Be system, except for samples MA19-23, 25, and 26, which deviate from this trend.

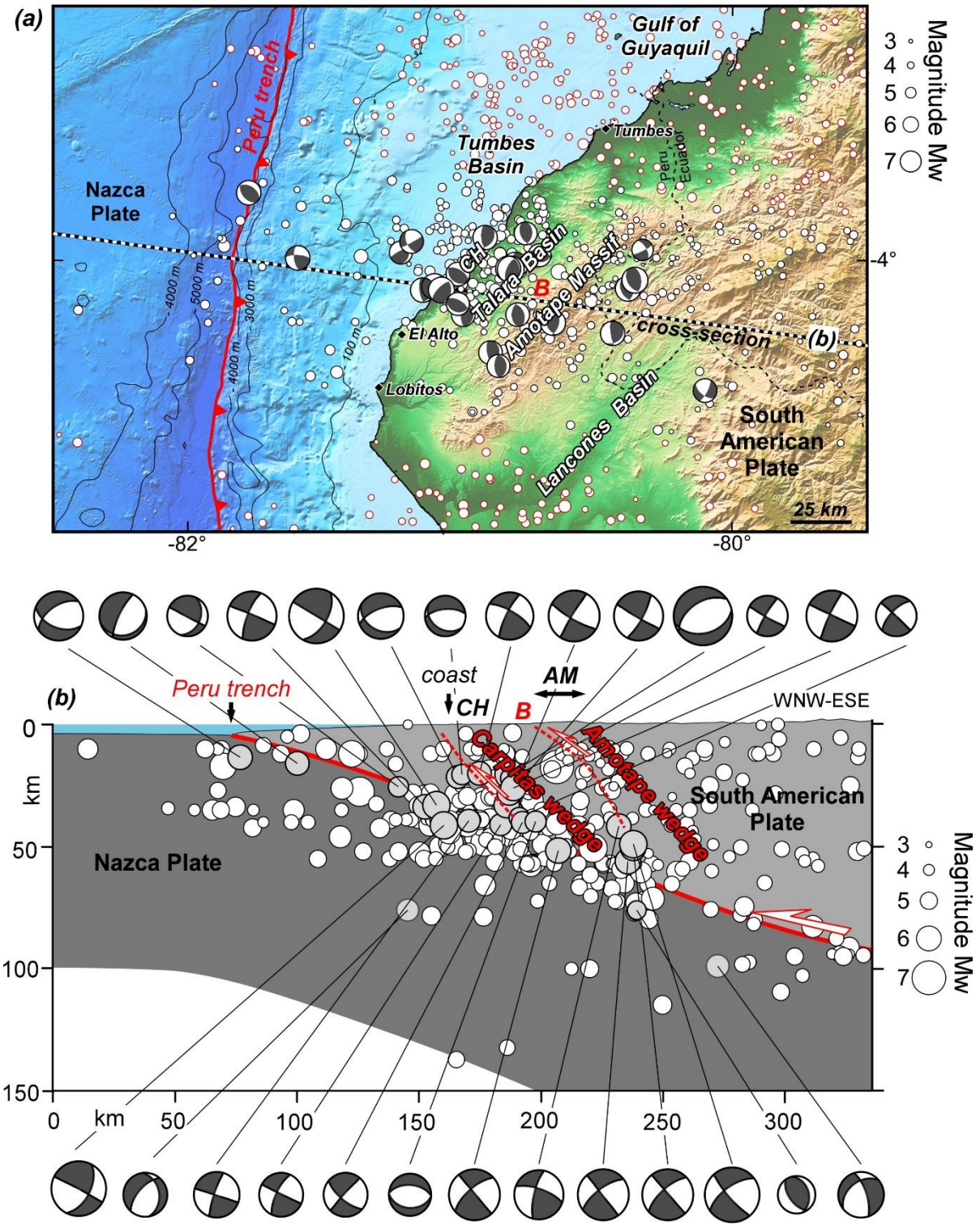

Fig. 10. (a) Map of the regional seismicity distribution and calculated focal mechanisms. Data are from ISC catalogs for the period 1970-2023. (b) Seismicity cross-section across the north Peruvian margin. The width of the cross-section is 50 km on either side of the cross-section axis (black circles are plotted on the cross-section). Focal mechanisms are shown in side view. CH: Carpitas High B: Breita area; AM: Amotape massif. See text for further explanations.

(a) **^{10}Be and ^{26}Al concentrations and the ratios ^{26}Al/^{10}Be along the Amotape massif**

Sample name	*Latitude (°S)*	*Longitude (°W)*	*Altitude (m)*	*Shielding factor*	*^{10}Be (at.g^{-1})*	*^{10}Be ± (at.g^{-1})*	*^{26}Al (at.g^{-1})*	*^{26}Al ± (at.g^{-1})*	*^{26}Al/^{10}Be*
MA19-15	4.258615	80.881187	260.90	0.99	114 164	3 919	726 250	33 588	6.361 ± 0.22
MA19-16	4.258259	80.883134	241.91	0.99	107 540	3 347	603 860	28 421	5.615 ± 0.20
MA19-17	4.260044	80.883389	247.10	0.99	125 122	9 840	831 776	34 816	6.648 ± 0.21
MA19-23	4.030072	80.612428	286.38	0.98	175 983	6 204	843 177	48 257	4.791 ± 0.11
MA19-24	4.029883	80.612311	286.63	0.98	145 404	4 491	985 481	51 142	6.778 ± 0.18
MA19-25	4.029798	80.612611	286.38	0.98	104 707	3 349	556 786	41 444	5.220 ± 0.20
MA19-26	4.029876	80.612775	286.63	0.98	172 956	7 046	556 980	52 057	3.220 ± 0.07

(b) **^{10}Be and ^{26}Al exposures ages and denudation rates along the Amotape massif**

Sample name	*Sample type*	*Min. exposure Age based on ^{10}Be (ka)*	*Maximum denudation rate (m/ka)*	*Min. exposure Age based on ^{26}Al (ka)*	*Maximum denudation rate (m/ka)*
MA19-15	Quartzite	39.6 ± 1.3	19.1 ± 0.6	36.3 ± 1.6	23.0 ± 1.0
MA19-16	Quartzite	37.9 ± 1.1	20.7 ± 0.6	30.5 ± 1.4	27.7 ± 1.3
MA19-17	Quartzite	44.0 ± 3.5	17.6 ± 1.3	42.2 ± 1.9	19.5 ± 0.8
MA19-23	Arenitic soil	59.3 ± 2.0	15.8 ± 0.5	41.6 ± 2.3	19.8 ± 1.1
MA19-24	Arenitic soil	48.9 ± 1.5	19.5 ± 0.6	48.9 ± 2.5	16.5 ± 0.8
MA19-25	Boulder	35.1 ± 1.1	22.4 ± 0.7	27.2 ± 2.0	31.2 ± 2.3
MA19-26	Boulder	58.4 ± 2.3	12.9 ± 0.5	27.3 ± 2.5	31.2 ± 2.9

Table 1. (a) Samples information, measured TCNs concentrations for ^{10}Be and ^{26}Al cosmogenic nuclides and ^{26}Al/^{10}Be ratios. (b) ^{10}Be and ^{26}Al minimum exposure ages and maximum denudation rates along the Amotape massif for each sample.

***(a)* ^{10}Be and ^{26}Al concentrations and the ratios ^{26}Al/^{10}Be along the Amotape massif**

Sample name	***Latitude (°S)***	***Longitude (°W)***	***Altitude (m)***	***Shielding factor***	***^{10}Be (at.g^{-1})***	***^{10}Be ± (at.g^{-1})***	***^{26}Al (at.g^{-1})***	***^{26}Al ± (at.g^{-1})***	***^{26}Al/^{10}Be***
MA19-15	4.258615	80.881187	260.90	0.99	114 164	3 919	726 250	33 588	6.361 ± 0.22
MA19-16	4.258259	80.883134	241.91	0.99	107 540	3 347	603 860	28 421	5.615 ± 0.20
MA19-17	4.260044	80.883389	247.10	0.99	125 122	9 840	831 776	34 816	6.648 ± 0.21
MA19-23	4.030072	80.612428	286.38	0.98	175 983	6 204	843 177	48 257	4.791 ± 0.11
MA19-24	4.029883	80.612311	286.63	0.98	145 404	4 491	985 481	51 142	6.778 ± 0.18
MA19-25	4.029798	80.612611	286.38	0.98	104 707	3 349	556 786	41 444	5.220 ± 0.20
MA19-26	4.029876	80.612775	286.63	0.98	172 956	7 046	556 980	52 057	3.220 ± 0.07

(b) ^{10}Be and ^{26}Al exposure ages and denudation rates along the Amotape massif

Sample name	***Sample type***	***Min. exposure Age based on 10Be (ka)***	***Maximum denudation rate (m/ka)***	***Min. exposure Age based on 26Al (ka)***	***Maximum denudation rate (m/ka)***
MA19-15	Quartzite	39.6 ± 1.3	19.1 ± 0.6	36.3 ± 1.6	23.0 ± 1.0

MA19-16	Quartzite	37.9 ± 1.1	20.7 ± 0.6	30.5 ± 1.4	27.7 ± 1.3
MA19-17	Quartzite	44.0 ± 3.5	17.6 ± 1.3	42.2 ± 1.9	19.5 ± 0.8
MA19-23	Arenitic soil	59.3 ± 2.0	15.8 ± 0.5	41.6 ± 2.3	19.8 ± 1.1
MA19-24	Arenitic soil	48.9 ± 1.5	19.5 ± 0.6	48.9 ± 2.5	16.5 ± 0.8
MA19-25	Boulder	35.1 ± 1.1	22.4 ± 0.7	27.2 ± 2.0	31.2 ± 2.3
MA19-26	Boulder	58.4 ± 2.3	12.9 ± 0.5	27.3 ± 2.5	31.2 ± 2.9

Supplementary material 1.

Site name	Latitude (°S)	Longitude (°W)	Altitude (m)	Age/Lithology	Number of faults	σ_1		σ_2		σ_3		ANG	RUP	Φ	Stress regime
						Trend	Plunge	Trend	Plunge	Trend	Plunge				
Site 1	4.21666	80.8833	149.00	Eocene/Conglomerates-sandstones	5	144	4	234	4	84	81	9	33	0.516	compressional
Site 2	4.22915	80.8911	160.00	Eocene/Conglomerates-sandstones	8	144	1	234	3	37	87	4	28	0.484	compressional
Site 3	4.22904	80.8899	164.00	Eocene/Conglomerates-sandstones	6	316	6	225	7	225	7	4	32	0.476	compressional

Supplementary material 2.

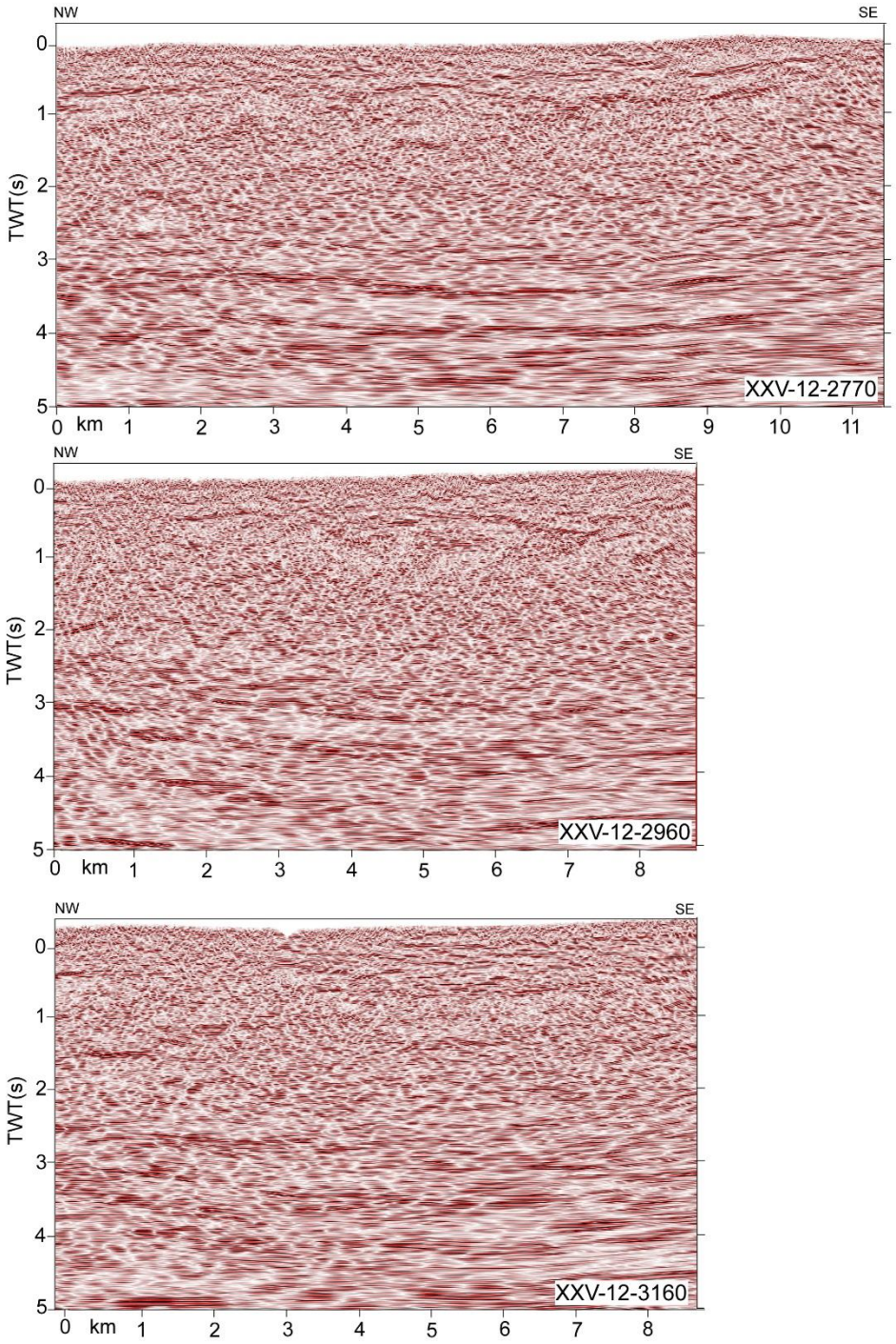

Supplementary material 4.

Analytical preparation data for 10Be and 26Al cosmogenic nuclide measurements

Sample name	Dissolved Quartz mass (g)	^{9}Be spike mass (mg)	^{9}Be spike (at.)	Tube weight (g)	Spike ^{9}Be and tube total weight (g)	Aliquot	Total ICP mass (g)
MA19-15	17.213	0.457100	3.045×10^{19}	12.914	29.015	0.212	10.3462
MA19-16	17.565	0.454200	3.026×10^{19}	13.350	29.547	0.220	10.4287
MA19-17	18.493	0.445200	2.966×10^{19}	13.438	29.168	0.208	10.3338
MA19-23	18.300	0.154900	3.131×10^{19}	13.134	28.236	0.206	10.2974
MA19-24	20.172	0.155000	3.133×10^{19}	12.969	28,661	0.207	10.3073
MA19-25	19.170	0.155200	3.137×10^{19}	12.993	29.981	0.207	10.2864
MA19-26	16.803	0.154500	3.123×10^{19}	13.120	32.256	0.207	10.2866

(a) ^{10}Be and ^{26}Al exposure ages and denudation rates along the Amotape massif

Declaration of interests

☒ The authors declare that they have no known competing financial interests or personal relationships that could have appeared to influence the work reported in this paper.

☐ The authors declare the following financial interests/personal relationships which may be considered as potential competing interests:

Andrea Peuzin reports was provided by University of Côte d'Azur. Andrea Peuzin reports a relationship with University of Côte d'Azur that includes: employment.

Graphical Abstract

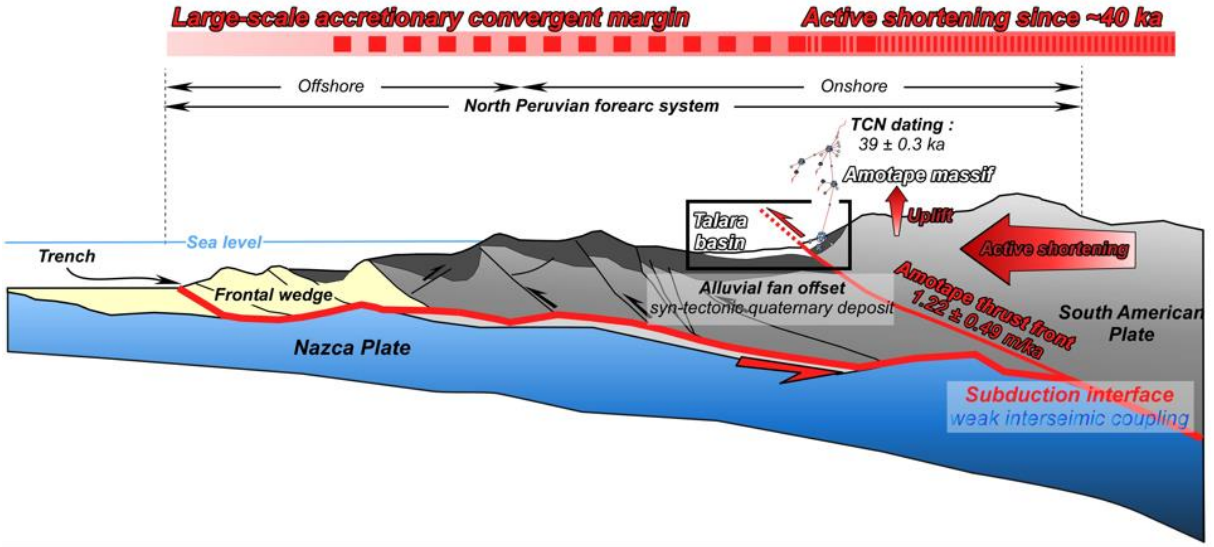

Highlights:

- First *in-situ* produced Terrestrial Cosmogenic Nuclides dating of deformed alluvial fans in the North Peruvian forearc.
- The Amotape massif is a basement-involved triangle zone, active during the late Pleistocene.
- We estimate a slip rate of 1.15 ± 0.46 m/ka for the Amotape thrust, since ~40 ka